Received: 19 May 2020 | Accepted: 18 October 2020

DOI: 10.1002/nme.6592

RESEARCH ARTICLE

WILEY

Rot-free mixed finite elements for gradient elasticity at finite strains

Johannes Riesselmann[1] | **Jonas W. Ketteler**[2] | **Mira Schedensack**[2] | **Daniel Balzani**[1]

[1]Chair of Continuum Mechanics, Ruhr University Bochum, Bochum, Germany

[2]Institute of Mathematics, Leipzig University, Leipzig, Germany

Correspondence
Daniel Balzani, Chair of Continuum Mechanics, Ruhr University Bochum, Bochum, Germany.
Email: daniel.balzani@rub.de

Funding information
Deutsche Forschungsgemeinschaft, Grant/Award Numbers: BA2823/15-1, SCHE1885/1-1

Abstract

Through enrichment of the elastic potential by the second-order gradient of deformation, gradient elasticity formulations are capable of taking nonlocal effects into account. Moreover, geometry-induced singularities, which may appear when using classical elasticity formulations, disappear due to the higher regularity of the solution. In this contribution, a mixed finite element discretization for finite strain gradient elasticity is investigated, in which instead of the displacements, the first-order gradient of the displacements is the solution variable. Thus, the C^1 continuity condition of displacement-based finite elements for gradient elasticity is relaxed to C^0. Contrary to existing mixed approaches, the proposed approach incorporates a rot-free constraint, through which the displacements are decoupled from the problem. This has the advantage of a reduction of the number of solution variables. Furthermore, the fulfillment of mathematical stability conditions is shown for the corresponding small strain setting. Numerical examples verify convergence in two and three dimensions and reveal a reduced computing cost compared to competitive formulations. Additionally, the gradient elasticity features of avoiding singularities and modeling size effects are demonstrated.

KEYWORDS

finite strains, gradient elasticity, higher-order gradients, mixed finite elements, size effects

1 | INTRODUCTION

The elastic potential in classical solid mechanical modeling is usually a functional of the first order gradient of deformation. Both in small strain and in finite strain elasticity this approach is sufficient for many applications. However, they do not take into account the finite resolution of the microstructure of the material. If the modeled geometry has, for example, sharp corners this can lead to nonphysical singularities of the strains and stresses resulting from these local models. In consequence, corresponding finite element simulations yield results, which are dependent on the mesh size around these singularities and numerical problems may arise. Due to the local nature of the classical elasticity formulations, the influence of material heterogeneities on the global elastic behavior is not taken into account. This becomes relevant when modeling specialized materials (such as metamaterials), in which material heterogeneities approach the scale of the macroscopic mechanical fields. Nonlocal approaches such as gradient elasticity, where the elastic potential is

enriched by a dependency on the second-order displacement gradient represent a remedy in these cases. Although nonlocal approaches have been in existence for many years, due to recent developments of specialized materials, the research of formulations has experienced an increased interest.

Various generalized continuum models are based on the theory of the Cosserat brothers,[1] in which rotational degrees of freedom derived from the balance of angular momentum at the material point are considered in order to take into account nonlocal effects. Recent contributions have been made in this field (such as Reference 2, among several others). In the frequently cited, more general theory of Reference 3, microdeformations are used to take into account microstructural effects on the material behavior. As a special case, in Reference 3 the second-order gradient elasticity approach is introduced. In this case, microstuctural effects are modeled through the enhancement of the elastic potential by a dependency on second-order gradients of displacements. For an overview of gradient elasticity approaches the reader is referred to Reference 4 (see also Reference 5 for a classification with respect to other nonlocal models). While the gradient elasticity approach itself is rather straightforward, a remaining research challenge is the identification and physical interpretation of the additional constitutive parameters that are appearing in the gradient elasticity formulation. Recent developments have been made by Reference 6 in which a determination of the parameters based on action principles has been proposed (see also Reference 7). Another field of study which has experienced recent increase of interest is the development of models, which incorporate flexoelectric effects. In these models, second-order displacement gradients are coupled with electric polarization fields, which are of increasing interest in the research of nanoelectronics and nanowire semiconductors.[8]

The main challenge in the development of numerical solution procedures for gradient-enhanced models is the increased continuity requirement for the interpolation functions of the solution fields, namely, C^1 continuity requirement for displacement-based finite elements. Straightforward corresponding C^1-continuous finite elements require high polynomial orders of the interpolation functions and additional element degrees of freedom corresponding to the gradients of the solution fields. An investigation of a C^1-continuous finite element formulation for gradient elasticity can be found in Reference 9. Another common approach is the use of isogeometric analysis (IGA) as discretization scheme. See Reference 10 for an IGA model for finite strain gradient elasticity, whereas in References 11 and 12 flexoelectric material behavior is modeled. While the realization of the C^1 continuity condition is straightforward with IGA, the discretization of complex (practically relevant) structures remain a challenge. Alternatively, mixed finite elements can be used. Through the introduction of additional mixed solution variables C^0-continuous interpolation functions can be used. In Reference 13 a mixed finite element formulation is investigated, which incorporates both displacements and Mindlins microdeformations as solution variables. In the rather recent contribution of Reference 14 various finite element discretizations incorporating the displacement and strain field as solution variables are investigated in a two-dimensional (2D) linear small strain setting. Another small strain finite element approach is introduced in Reference 15, where both first and second displacement gradients are introduced as mixed variables and corresponding numerical investigations focus on the incorporation of point and line forces. The small strain two-dimensional (2D) and three-dimensional (3D) mixed formulations of References 16 and 17, respectively, incorporate displacements, displacement gradients and Lagrange multipliers as solution variables. For a corresponding mathematical investigation with respect to inf-sup stability and an extension to finite strains see Reference 18. So far, the main challenges of these existing mixed formulations is the computational costliness due to a large number of degrees of freedom and the lack of discrete inf-sup stability in some cases.

In this contribution a decoupled approach, based on the polyharmonic operator splitting approach of Reference 19, is investigated for the hyperelastic finite-strain gradient elasticity problem. In Section 3.1 the continuous large deformation variational formulation is introduced. Specifically, the case is examined in which the constitutive parameter corresponding to the nonlocal part of the formulation is significantly smaller than for the local part. Through a stabilization term, a loss of stability in this case (as also apparent in the existing non-decoupled mixed approaches of Reference 18, following References 16 and 17) can be avoided. In the following Section 3.2 several finite element discretizations, both in 2D and in 3D, are investigated. Numerical experiments (Section 4) verify convergence of the proposed formulations. In the 2D case a cost reduction compared to the nondecoupled mixed approach of Reference 18 (which is based on References 16 and 17) is shown. Furthermore, the gradient elasticity features of avoiding singularities and modeling size effects are illustrated.

2 | FUNDAMENTALS

Section 2.1 gives preliminary remarks on notation, finite strain kinematics, and the Helmholtz decomposition, which is used for the decomposed Lagrange multiplier method introduced in Section 3. An overview on the continuum mechanical framework of the gradient elasticity approach is given in Section 2.4.

2.1 | Tensor operations

For the dimension $d \in \{2, 3\}$ let $\boldsymbol{T}^{(n)}$ be a tensor-valued function of order $n \in \mathbb{N}_0$ over $(\mathbb{R}^d)^n$. We define the scalar product $\boldsymbol{T} \cdot \boldsymbol{T} : (\mathbb{R}^d)^n \times (\mathbb{R}^d)^n \to \mathbb{R}^n$. Let $\wedge$ denote the cross product, which is applied row-wise to tensor-valued functions. Explicitly, the cross products of a second-order tensor $\boldsymbol{T}$ and a vector $\boldsymbol{s}$ take the forms

$$\boldsymbol{T} \wedge \boldsymbol{s} = \begin{bmatrix} T_{13}s_2 - T_{12}s_3 & T_{11}s_3 - T_{13}s_1 & T_{12}s_1 - T_{11}s_2 \\ T_{23}s_2 - T_{22}s_3 & T_{21}s_3 - T_{23}s_1 & T_{22}s_1 - T_{21}s_2 \\ T_{33}s_2 - T_{32}s_3 & T_{31}s_3 - T_{33}s_1 & T_{32}s_1 - T_{31}s_2 \end{bmatrix} \text{ and } \boldsymbol{T} \wedge \boldsymbol{s} = \begin{bmatrix} T_{12}s_1 - T_{11}s_2 \\ T_{22}s_1 - T_{21}s_2 \end{bmatrix}, \tag{1}$$

for $d = 3$ and $d = 2$, respectively. We define the row-wise applied derivative operators

$$\nabla \boldsymbol{T}^{(n)} := \partial_j T_{i_1 \dots i_n} \boldsymbol{e}_{i_1} \otimes \dots \otimes \boldsymbol{e}_{i_n} \otimes \boldsymbol{e}_j, \tag{2}$$

$$\operatorname{Div} \boldsymbol{T}^{(n)} := \partial_{i_n} T_{i_1 \dots i_n} \boldsymbol{e}_{i_1} \otimes \dots \otimes \boldsymbol{e}_{i_{n-1}}, \tag{3}$$

$$\operatorname{Rot} \boldsymbol{T}^{(n)} := -\partial_j T_{i_1 \dots i_n} \boldsymbol{e}_{i_1} \otimes \dots \otimes \boldsymbol{e}_{i_n} \wedge \boldsymbol{e}_j, \tag{4}$$

where $\boldsymbol{e}_{i_{(\bullet)}}$ denote Cartesian base vectors.

2.2 | Finite strain kinematics

For each position vector $\boldsymbol{X} \in \mathcal{B}$ of a material point in the reference configuration there exists a corresponding position vector $\boldsymbol{x} \in \mathcal{S}$ in the deformed configuration defined by the deformation map $\boldsymbol{\varphi} : \mathcal{B} \to \mathcal{S}$. Through $\boldsymbol{\varphi}(\boldsymbol{X}, t) = \boldsymbol{X} + \boldsymbol{u}(\boldsymbol{X}, t)$, the deformation map can be described in terms of the displacement function $\boldsymbol{u}$. We denote the deformation gradient by

$$\boldsymbol{F} = \nabla \boldsymbol{\varphi} = \boldsymbol{1} + \nabla \boldsymbol{u}. \tag{5}$$

Within the scope of this contribution all derivative operators are with respect to coordinates in the reference configuration.

2.3 | Helmholtz decomposition

Let $\mathcal{B}$ be a bounded, simply connected domain. Then, a second-order tensor function $\boldsymbol{\Lambda}$ can be decomposed (see Reference 20, corollary 2.31) into a solenoidal (divergence-free) part $\boldsymbol{\Lambda}_{\mathrm{c}}$ and an irrotational (rot-free) part $\boldsymbol{\Lambda}_{\mathrm{g}}$:

$$\boldsymbol{\Lambda} = \boldsymbol{\Lambda}_{\mathrm{c}} + \boldsymbol{\Lambda}_{\mathrm{g}}. \tag{6}$$

Consequently, the two parts can be expressed by gradient and rotation functions, respectively:

$$\boldsymbol{\Lambda}_{\mathrm{c}} = \operatorname{Rot} \boldsymbol{\Phi} \quad \text{and} \quad \boldsymbol{\Lambda}_{\mathrm{g}} = -\nabla \boldsymbol{g}, \tag{7}$$

with $\boldsymbol{g} \in H_0^1$ being a vector-valued function and $\boldsymbol{\Phi} \in \mathcal{Q}$, where $\mathcal{Q}$ is the space of vector-valued L^2 functions with vanishing integral mean for $d = 2$, while $\mathcal{Q}$ is the space for tensor-valued L^2 functions with vanishing divergence and normal boundary conditions for $d = 3$; see Section 3.1.6 for details.

2.4 | Gradient elasticity theory

When considering a gradient-elastic boundary value problem, the boundary of a given body $\mathcal{B}$ can be decomposed as follows: $\partial\mathcal{B} = \Gamma_D \cup \Gamma_N = \Gamma_H \cup \Gamma_M$. Here, Γ_D and Γ_N denote the standard Dirichlet- and Neumann boundary, while

Γ_H and Γ_M denote a Dirichlet- and Neumann boundary corresponding to higher-order quantities (cf. References 3,21). The gradient elasticity solution $\boldsymbol{u}$ is the minimizer of the elastic potential

$$\Pi[\boldsymbol{u}] = \Pi^{\text{int}}[\boldsymbol{u}] + \Pi^{\text{ext}}[\boldsymbol{u}] \Rightarrow \min_{\boldsymbol{u}}, \quad \text{with} \tag{8}$$

$$\Pi^{\text{int}}[\boldsymbol{u}] = \int_{\mathcal{B}} \psi(\boldsymbol{F}(\nabla\boldsymbol{u}), \nabla\boldsymbol{F}(\nabla\boldsymbol{u}))\mathrm{d}V, \tag{9}$$

$$\Pi^{\text{ext}}[\boldsymbol{u}] = -\int_{\mathcal{B}} \boldsymbol{u}\cdot\boldsymbol{f}\,\mathrm{d}V - \int_{\Gamma_N} \boldsymbol{u}\cdot\boldsymbol{t}\,\mathrm{d}A - \int_{\Gamma_M} \nabla\boldsymbol{u}\,\boldsymbol{N}\cdot\boldsymbol{r}\,\mathrm{d}A. \tag{10}$$

Here, Π^{int} denotes the volume integral of the internal elastic energy density ψ. Π^{ext} denotes the external potential of volume load $\boldsymbol{f}$ and surface traction $\boldsymbol{t}$. Due to the appearance of second order displacement gradients in (8), the minimizer is sought to be in the Sobolev space H^2 of twice differentiable functions. Moreover we denote the displacement boundary $\boldsymbol{u} = \overline{\boldsymbol{u}}$ and $\nabla\boldsymbol{u}\wedge\boldsymbol{N} = \nabla\overline{\boldsymbol{u}}\wedge\boldsymbol{N}$ on Γ_D and $\nabla\boldsymbol{u}\,\boldsymbol{N} = \nabla\overline{\boldsymbol{u}}\,\boldsymbol{N}$ on Γ_H. Here $\boldsymbol{N}$ denotes the unit normal surface vector of the body in reference configuration and $\overline{\boldsymbol{u}}$ denotes a prescribed displacement function. In what follows, the higher order surface traction vector (cf. Reference 10, see also Reference 3) $\boldsymbol{r} = \boldsymbol{0}$ is assumed to be homogeneous on Γ_M. Applying the stationarity condition leads to the following variational problem: For given $\boldsymbol{f}$, $\boldsymbol{t}$, and the previously discussed essential boundary conditions, find $\boldsymbol{u} \in H^2$ such that

$$\int_{\mathcal{B}} (\nabla\delta\boldsymbol{u}\cdot\boldsymbol{P} + \nabla^2\delta\boldsymbol{u}\cdot\boldsymbol{G})\,\mathrm{d}V = -\Pi^{\text{ext}}[\delta\boldsymbol{u}], \tag{11}$$

for all $\delta\boldsymbol{u}$. Here, we denote $\nabla^2(\bullet) := \nabla(\nabla(\bullet))$ as the second-order gradient and introduce the first- and second-order stress tensors $\boldsymbol{P} := \partial_{\boldsymbol{F}}\psi$ and $\boldsymbol{G} := \partial_{\nabla\boldsymbol{F}}\psi$, respectively.

3 | THE ROT-FREE MIXED FORMULATION

This section introduces a finite strain mixed finite element approach, in which, through a rot-free constraint, the displacement and displacement gradient solution variables appear in a decoupled set of variational equations promising increased computational efficiency. While Section 3.1 discusses the continuous variational setting, in Section 3.2 suitable finite element interpolations are discussed and the corresponding set of discrete matrix-vector notations are obtained on the element level. The proposed approaches are complemented by a mathematical analysis of the small strain counterparts in Sections 3.1.6 and 3.2.5 for the continuous and the discrete setting, respectively.

3.1 | Continuous variational framework

In the following it is assumed that the body $\mathcal{B}$ has a finite size and is simply connected with a connected essential boundary Γ_D.

3.1.1 | Decomposed Lagrange multiplier method

In order to arrive at a formulation, which contains only first order gradients and thus, enables C^0 continuous finite elements, the total elastic potential (8) is reformulated to the following Lagrangian:

$$\Pi[\boldsymbol{u}, \boldsymbol{H}, \boldsymbol{\Lambda}] = \Pi^{\text{int}}[\boldsymbol{H}] + \Pi^{\text{ext}}[\boldsymbol{u}] + \Pi^{\text{lag}}[\boldsymbol{u}, \boldsymbol{H}, \boldsymbol{\Lambda}] \quad \text{with} \tag{12}$$

$$\Pi^{\text{lag}} = \int_{\mathcal{B}} \boldsymbol{\Lambda}\cdot(\boldsymbol{H} - \nabla\boldsymbol{u})\,\mathrm{d}V. \tag{13}$$

Here, the internal elastic potential Π^{int} is a functional of the displacement gradient variable $\boldsymbol{H}$ and compatibility with the displacement $\boldsymbol{u}$ is enforced by the constraint term Π^{lag} (13). The Lagrange multiplier $\boldsymbol{\Lambda} = -\nabla\boldsymbol{g} + \operatorname{Rot}\boldsymbol{\Phi}$ is decomposed

according to relations (6) and (7) into a gradient and a rotation. Thus, by making use of the divergence theorem, (13) can be written as

$$\Pi^{\text{lag}} = \int_{\mathcal{B}} [\nabla \boldsymbol{g} \cdot (\nabla \boldsymbol{u} - \boldsymbol{H}) + \boldsymbol{\Phi} \cdot \operatorname{Rot} \boldsymbol{H}] \, \mathrm{d}V. \tag{14}$$

Note the exclusion of $\nabla \boldsymbol{u}$ in the second term of (14), since the scalar product of rot and gradient tensor functions vanishes. The second term of (14) can be interpreted as constraint term enforcing $\boldsymbol{H}$ to be rot-free, which is a necessary condition for gradient functions.

Remark 1. In the case of a vanishing nonlocal contribution of the strain energy density ($\boldsymbol{G} = \boldsymbol{0}$), $\boldsymbol{\Lambda}$ can be identified as the first Piola Kirchhoff stress tensor $\boldsymbol{P}$ and $-\nabla \boldsymbol{g} + \operatorname{Rot} \boldsymbol{\Phi}$ can be viewed as corresponding split of the latter. This can be verified by the Euler–Lagrange equations from variation of (12) according to the Hu–Washizu variational principle.[22]

3.1.2 | Stabilization for the limit case of vanishing nonlocal contribution

In order to take into account the case in which the nonlocal contribution becomes small, the stabilization term

$$\Pi^{\text{stab}} = \int_{\mathcal{B}} \frac{\alpha}{2} (\operatorname{Rot} \boldsymbol{H})^2 \, \mathrm{d}V, \tag{15}$$

is added to (12). Through adding this augmentation term, the problem remains well posed even in the limit case of vanishing nonlocal contribution and the inf-sup stability condition is fulfilled. The problem (12) is not changed by the stabilization term since the solution satisfies $\delta_{\boldsymbol{H}} \Pi^{\text{stab}} = 0$. A corresponding mathematical analysis can be found in Section 3.1.6.

3.1.3 | 2D variational formulation

In the 2D case $d = 2$ with definition (4) $\operatorname{Rot} \boldsymbol{H}$ simplifies to the vector

$$\operatorname{Rot} \boldsymbol{H} = \begin{bmatrix} \partial_{X_1} H_{12} - \partial_{X_2} H_{11} \\ \partial_{X_1} H_{22} - \partial_{X_2} H_{21} \end{bmatrix}. \tag{16}$$

Thus, in this case the Lagrange multiplier $\boldsymbol{\Phi}$ is also vector-valued and fulfills the inf-sup stability condition (cf. (B1) in Section 3.1.6) without further restrictions with respect to differential operations, namely as element of the Sobolev space L^2 with a fixed mean integral value $\int_{\mathcal{B}} \boldsymbol{\Phi} \, \mathrm{d}V = 0$. With (12), (14), and (15) the weak form corresponding to the Lagrangian $\Pi = \Pi^{\text{int}} + \Pi^{\text{ext}} + \Pi^{\text{lag}} + \Pi^{\text{stab}}$ reads

$$\delta_{\boldsymbol{u}} \Pi = 0 = \int_{\mathcal{B}} \nabla \delta \boldsymbol{u} \cdot \nabla \boldsymbol{g} \, \mathrm{d}V + \Pi^{\text{ext}}[\delta \boldsymbol{u}], \tag{17}$$

$$\delta_{\boldsymbol{H}} \Pi = 0 = \int_{\mathcal{B}} (\delta \boldsymbol{H} \cdot \boldsymbol{P} + \nabla \delta \boldsymbol{H} \cdot \boldsymbol{G} + \operatorname{Rot} \delta \boldsymbol{H} \cdot \boldsymbol{\Phi} + \alpha \operatorname{Rot} \delta \boldsymbol{H} \cdot \operatorname{Rot} \boldsymbol{H} - \delta \boldsymbol{H} \cdot \nabla \boldsymbol{g}) \, \mathrm{d}V, \tag{18}$$

$$\delta_{\boldsymbol{\Phi}} \Pi = 0 = \int_{\mathcal{B}} \delta \boldsymbol{\Phi} \cdot \operatorname{Rot} \boldsymbol{H} \, \mathrm{d}V, \tag{19}$$

$$\delta_{\boldsymbol{g}} \Pi = 0 = \int_{\mathcal{B}} \nabla \delta \boldsymbol{g} \cdot (\nabla \boldsymbol{u} - \boldsymbol{H}) \, \mathrm{d}V. \tag{20}$$

We seek $\boldsymbol{u}$ and $\boldsymbol{g}$ in the Sobolev space $H^1 := \{\delta \boldsymbol{u} \in L^2 : \nabla \delta \boldsymbol{u} \in L^2\}$ for all $\delta \boldsymbol{u}, \delta \boldsymbol{g} \in H^1$. Moreover, we use Dirichlet boundary conditions $\boldsymbol{u} = \overline{\boldsymbol{u}}$ and $\boldsymbol{g} = \boldsymbol{0}$ on Γ_D with $\overline{\boldsymbol{u}}$ being the prescribed displacement. Corresponding to the displacement boundary, the tangential direction of the displacement gradient variable is prescribed on Γ_D with $\boldsymbol{H} \wedge \boldsymbol{N} = \nabla \overline{\boldsymbol{u}} \wedge \boldsymbol{N}$, where $\boldsymbol{N}$ denotes the surface normal vector in the reference configuration. The displacement gradient variable $\boldsymbol{H} \in H^{1(2)}$

is sought for all $\delta \boldsymbol{H} \in H^{1(2)}$. Furthermore, the normal direction of the displacement gradient corresponding to the higher-order essential boundary is prescribed by $\boldsymbol{H}\,\boldsymbol{N} = \nabla \overline{\boldsymbol{u}}\,\boldsymbol{N}$ on Γ_H.

Remark 2. The equation system (17) through (20) depicts a split of the second-order weak form (11) into a set of first-order equations. (cf. Reference 19, where this approach was proposed for polyharmonic problems). In the present system of equations, the displacement $\boldsymbol{u}$ is decoupled from the main problem (18) and constraint Equation (19). The displacements only appear in the simple Laplace-type Equations (17) and (20). In the following, (17) and (20) are referred to as pre- and postprocessing step, respectively. This set of equations follows first ideas in Reference 23 in the context of discretizing Kirchhoff's equations of thin plate bending by C0 finite elements. Note, that the higher-order tractions $\boldsymbol{r}$, which were assumed to be zero could also be applied through extending (18) correspondingly.

3.1.4 | 3D variational formulation

In the 3D case $d = 3$, to fulfill the inf-sup condition, the Lagrange multiplier $\boldsymbol{\Phi}$ needs to be divergence-free, namely it needs to be an element of the Sobolev space, that is, $\boldsymbol{\Phi} \in H(\mathrm{Div}^0)^{(2)}$ with vanishing boundary trace $\boldsymbol{\Phi N} = \boldsymbol{0}$ on Γ_D (cf. Proposition 7). Thus, in this case, the second divergence-free constraint term

$$\Pi^{\mathrm{div}} = \int_{\mathcal{B}} \boldsymbol{\mu} \cdot \mathrm{Div}\, \boldsymbol{\Phi}\, \mathrm{d}V, \tag{21}$$

is added to (12), where $\boldsymbol{\mu}$ is a vector-valued, second Lagrange multiplier. For $\boldsymbol{\mu}$ the space L^2 and a fixed mean integral value $\int_B \boldsymbol{\mu}\, \mathrm{d}V = 0$ is a suitable choice (cf. (39) and Proposition 3). Similar to the previous case, together with (21), the weak form corresponding to the Lagrangian $\Pi = \Pi^{\mathrm{int}} + \Pi^{\mathrm{ext}} + \Pi^{\mathrm{lag}} + \Pi^{\mathrm{stab}} + \Pi^{\mathrm{div}}$ reads

$$\delta_{\boldsymbol{H}} \Pi = 0 = \int_{\mathcal{B}} (\delta \boldsymbol{H} \cdot \boldsymbol{P} + \nabla \delta \boldsymbol{H} \cdot \boldsymbol{G} + \mathrm{Rot}\, \delta \boldsymbol{H} \cdot \boldsymbol{\Phi} + \alpha\, \mathrm{Rot}\, \delta \boldsymbol{H} \cdot \mathrm{Rot}\, \boldsymbol{H} - \delta \boldsymbol{H} \cdot \nabla \boldsymbol{g})\, \mathrm{d}V, \tag{22}$$

$$\delta_{\boldsymbol{\Phi}} \Pi = 0 = \int_{\mathcal{B}} (\delta \boldsymbol{\Phi} \cdot \mathrm{Rot}\, \boldsymbol{H} + \mathrm{Div}\, \delta \boldsymbol{\Phi} \cdot \boldsymbol{\mu})\, \mathrm{d}V, \tag{23}$$

$$\delta_{\boldsymbol{\mu}} \Pi = 0 = \int_{\mathcal{B}} \delta \boldsymbol{\mu} \cdot \mathrm{Div}\, \boldsymbol{\Phi}\, \mathrm{d}V, \tag{24}$$

and $\delta_{\boldsymbol{u}} \Pi$ and $\delta_{\boldsymbol{g}} \Pi$ according to (17) and (20), and the spaces for $\boldsymbol{u}, \boldsymbol{g}$, and $\boldsymbol{H}$ unchanged.

3.1.5 | Alternative 3D formulation

Starting point for an alternative approach is again the Lagrange multiplier decomposition of Section 3.1.1. However, the split takes the form $\boldsymbol{\Lambda} = -\nabla \boldsymbol{g} + \boldsymbol{\Lambda}_c$, where the variable $\boldsymbol{\Lambda}_c$ is sought to have the characteristics of a 3D rotational tensor field, namely to be divergence-free. Subsequently, the potentials (14) and (21) are modified as

$$\Pi^{\mathrm{lag}} = \int_{\mathcal{B}} [\nabla \boldsymbol{g} \cdot (\nabla \boldsymbol{u} - \boldsymbol{H}) + \boldsymbol{\Lambda}_c \cdot \boldsymbol{H}]\, \mathrm{d}V, \tag{25}$$

$$\Pi^{\mathrm{div}} = \int_{\mathcal{B}} \boldsymbol{\mu} \cdot \mathrm{Div}\, \boldsymbol{\Lambda}_c\, \mathrm{d}V. \tag{26}$$

Note, that in the second term of (25) only the rotation part of $\boldsymbol{H}$ is controlled by the Lagrange multiplier $\boldsymbol{\Lambda}_c$. This is due to the fact that with (26) $\boldsymbol{\Lambda}_c$ is specifically sought to be a rotation function and thus not having an influence on the divergence part of $\boldsymbol{H}$. Proceeding analogously to Section 3.1.4, we obtain the modified weak forms

$$\delta_{\boldsymbol{H}} \Pi = 0 = \int_{\mathcal{B}} (\delta \boldsymbol{H} \cdot \boldsymbol{P} + \nabla \delta \boldsymbol{H} \cdot \boldsymbol{G} + \delta \boldsymbol{H} \cdot \boldsymbol{\Lambda}_c + \alpha\, \mathrm{Rot}\, \delta \boldsymbol{H} \cdot \mathrm{Rot}\, \boldsymbol{H} - \delta \boldsymbol{H} \cdot \nabla \boldsymbol{g})\, \mathrm{d}V, \tag{27}$$

$$\delta_{\boldsymbol{\Phi}} \Pi = 0 = \int_{\mathcal{B}} (\delta \boldsymbol{\Lambda}_c \cdot \boldsymbol{H} + \mathrm{Div}\, \delta \boldsymbol{\Lambda}_c \cdot \boldsymbol{\mu})\, \mathrm{d}V, \tag{28}$$

$$\delta_{\boldsymbol{\mu}} \Pi = 0 = \int_{\mathcal{B}} \delta \boldsymbol{\mu} \cdot \operatorname{Div} \boldsymbol{\Lambda}_c \, \mathrm{d}V, \tag{29}$$

and $\delta_{\boldsymbol{u}} \Pi$ and $\delta_{\boldsymbol{g}} \Pi$ according to (17) and (20), and the spaces for $\boldsymbol{u}, \boldsymbol{g}$, and $\boldsymbol{H}$ unchanged. For $\boldsymbol{\Lambda}_c$ a zero trace on the Neumann boundary $\boldsymbol{\Lambda}_c \boldsymbol{N} = \boldsymbol{0}$ on Γ_N is prescribed.

3.1.6 | Mathematical analysis of the continuous formulations

In this section we prove the stability of the proposed approach in the small strain framework. Proofs of the propositions, lemmas, and corollaries of this section are given in Appendix B1. For the mathematical analysis it will be assumed that the displacements are small and the internal energy in (9) is additively decomposed into a term quadratic in $\nabla \boldsymbol{u}$ and a term quadratic in $\nabla^2 \boldsymbol{u}$. Let $L^2(\mathcal{B}, (\mathbb{R}^d)^n)$ denote the space of L^2 functions with values in $(\mathbb{R}^d)^n$ and define the L^2-inner product and the L^2-norm for an n-order tensor valued function $\boldsymbol{T} \in L^2(\mathcal{B}, (\mathbb{R}^d)^n)$ by

$$(\delta \boldsymbol{T}, \boldsymbol{T})_{L^2(\mathcal{B})} := \int_{\mathcal{B}} \delta \boldsymbol{T} \cdot \boldsymbol{T} \, \mathrm{d}V \quad \text{and} \quad ||\boldsymbol{T}||^2_{L^2(\mathcal{B})} := (\boldsymbol{T}, \boldsymbol{T})_{L^2(\mathcal{B})}. \tag{30}$$

We furthermore define the space

$$\mathcal{U} := \{\boldsymbol{u} \in H^2 \, : \, \boldsymbol{u}|_{\partial \mathcal{B}} = \boldsymbol{0} \ \text{and} \ \nabla \boldsymbol{u} \, \boldsymbol{N}|_{\partial \mathcal{B}} = \boldsymbol{0}\}. \tag{31}$$

For the left-hand side of (11) we define the bilinear form

$$a(\nabla \delta \boldsymbol{u}, \nabla \boldsymbol{u}) := (\operatorname{sym}(\nabla \delta \boldsymbol{u}), \mathbb{C} \, : \, \operatorname{sym}(\nabla \boldsymbol{u}))_{L^2(\mathcal{B})} + c_1 (\nabla^2 \delta \boldsymbol{u}, \nabla^2 \boldsymbol{u})_{L^2(\mathcal{B})}, \tag{32}$$

where $\mathbb{C}$ denotes a constant fourth-order elasticity tensor and $c_1 > 0$ a constitutive parameter associated with the higher order stress response. For a homogeneous boundary $\partial \mathcal{B} = \Gamma_D = \Gamma_H$ the small-strain gradient elasticity problem corresponding to (11) simplifies to finding $\boldsymbol{u} \in \mathcal{U}$ for a given volume force $\boldsymbol{f} \in L^2$ so that

$$a(\nabla \delta \boldsymbol{u}, \nabla \boldsymbol{u}) = (\delta \boldsymbol{u}, \boldsymbol{f})_{L^2(\mathcal{B})} \quad \text{for all} \quad \delta \boldsymbol{u} \in \mathcal{U}. \tag{33}$$

For the mathematical investigation we define the spaces

$$\mathcal{G} := \{\delta \boldsymbol{g} \in H^m_0(\mathcal{B}; (\mathbb{R}^d)^1)\}, \tag{34}$$

$$\mathcal{V} := \{\delta \boldsymbol{H} \in H^m_0(\mathcal{B}; (\mathbb{R}^d)^2)\}, \tag{35}$$

where $H^m_0(\mathcal{B}; (\mathbb{R}^d)^n)$ denotes the H^m functions with values in $(\mathbb{R}^d)^n$ satisfying zero Dirichlet boundary conditions on $\partial \mathcal{B}$. Furthermore, the definition for the Lagrange multiplier involves the space $L^2_0(\mathcal{B}, (\mathbb{R}^d)^n)$ which denotes the $L^2(\mathcal{B}, (\mathbb{R}^d)^n)$ functions that satisfy $\int_{\mathcal{B}} \boldsymbol{T} \, \mathrm{d}V = 0$ for $d = 2$, while for $d = 3$ we define

$$H_0(\operatorname{Div}^0)^{(n)} := \{\boldsymbol{T} \in L^2(\mathcal{B}, (\mathbb{R}^d)^n) \, : \, \operatorname{Div} \boldsymbol{T} = \boldsymbol{0} \ \text{in} \ \mathcal{B} \ \text{and} \ \boldsymbol{T} \, \boldsymbol{N}|_{\partial \mathcal{B}} = \boldsymbol{0}\}. \tag{36}$$

Thus, we define $\mathcal{Q} := \{\delta \boldsymbol{\Phi} \in L^2_0(\mathcal{B}, (\mathbb{R}^d)^n) \ \text{if} \ d = 2\}$ or $\mathcal{Q} := \{\delta \boldsymbol{\Phi} \in H_0(\operatorname{Div}^0) \ \text{if} \ d = 3\}$.

We then define the bilinear form $b : \mathcal{V} \times \mathcal{Q} \to \mathbb{R}$ by

$$b(\delta \boldsymbol{H}, \delta \boldsymbol{\Phi}) := (\operatorname{Rot} \delta \boldsymbol{H}, \delta \boldsymbol{\Phi})_{L^2(\mathcal{B})}.$$

Define the bilinear form with added stabilization term $\tilde{a} : \mathcal{V} \times \mathcal{V} \to \mathbb{R}$ by

$$\tilde{a}(\boldsymbol{H}, \delta \boldsymbol{H}) := a(\boldsymbol{H}, \delta \boldsymbol{H}) + \alpha (\operatorname{Rot} \boldsymbol{H}, \operatorname{Rot} \delta \boldsymbol{H})_{L^2(\mathcal{B})}.$$

The small strain-analogon to (18) seeks $(\boldsymbol{H}, \boldsymbol{\Phi}) \in \mathcal{V} \times \mathcal{Q}$ for a given $\boldsymbol{g} \in \mathcal{G}$ such that

$$\tilde{a}(\boldsymbol{H}, \delta\boldsymbol{H}) + b(\delta\boldsymbol{H}, \boldsymbol{\Phi}) = (\nabla \boldsymbol{g}, \delta\boldsymbol{H})_{L^2(\mathcal{B})}$$
$$b(\boldsymbol{H}, \delta\boldsymbol{\Phi}) = 0, \tag{37}$$

for all $(\delta\boldsymbol{H}, \delta\boldsymbol{\Phi}) \in \mathcal{V} \times \mathcal{Q}$. We now show that (37) is stable and robust for $c_1 \to 0$. The robustness is proved with respect to the following norm on $\mathcal{V}$ that depends on the parameter c_1 that describes the nonlocal contribution,

$$|||\delta\boldsymbol{H}||| := \left(c_1 \|\mathrm{D}\delta\boldsymbol{H}\|^2_{L^2(\mathcal{B})} + \alpha \|\mathrm{Rot}\, \delta\boldsymbol{H}\|^2_{L^2(\mathcal{B})} + \|\mathbb{C}^{1/2}\, \mathrm{sym}\, \delta\boldsymbol{H}\|^2_{L^2(\mathcal{B})}\right)^{1/2}.$$

Note that, if $\mathrm{Rot}\, \boldsymbol{H} = 0$, then $\boldsymbol{H}$ is a gradient of a function in H^1_0. Therefore, Korn's inequality implies that for $\min\{c_1, \alpha\} > 0$ this is in fact a norm.

The following proposition proves the unique existence of solutions to (18) with stabilization in the linear strain case.

Proposition 1. *Let* $\max\{\alpha, c_1\} > c > 0$ *and* $\max\{\alpha, c_1\} < C < \infty$. *There exists a unique solution* $(\boldsymbol{H}, \boldsymbol{\Phi}) \in \mathcal{V} \times \mathcal{Q}$ *to the problem (37).*

Remark 3. Note that Proposition 1 remains true, if the stabilization term is not added to the bilinear form, that is, if $\tilde{a}$ is replaced by a in (37). This comes from the fact that functions in the kernel of b are rot free and a is coercive on this kernel. However, this is no longer true for the discretization and therefore, we include the stabilization term.

The following proposition states that the reformulated problem is in fact equivalent to the original problem.

Proposition 2. *If* $\boldsymbol{u} \in \mathcal{U}$ *is a solution of the original problem (33) then there exists* $\boldsymbol{\Phi} \in \mathcal{Q}$ *and* $\boldsymbol{g} \in \mathcal{G}$ *such that* $(\boldsymbol{u}, \nabla\boldsymbol{u}, \boldsymbol{\Phi}, \boldsymbol{g}) \in \mathcal{G} \times \mathcal{V} \times \mathcal{Q} \times \mathcal{G}$ *solves (17), (37) and (20). On the other hand, if* $(\boldsymbol{u}, \boldsymbol{H}, \boldsymbol{\Phi}, \boldsymbol{g}) \in \mathcal{G} \times \mathcal{V} \times \mathcal{Q} \times \mathcal{G}$ *solves (17), (37), and (20), then* $\boldsymbol{u}$ *solves (33).*

3.1.7 | Stability of the 3D variational formulation with two Lagrange multipliers

We now show that in the small-strain framework the solution of the 3D variational formulation (22) through (24) coincides with the solution of the original problem. Define the spaces of the Lagrange multipliers

$$\tilde{\mathcal{Q}} := \left\{\boldsymbol{\Phi} \in H_0(\mathrm{Div})^{(2)}\right\} \quad (\text{for } d = 3) \quad \text{and} \tag{38}$$

$$\mathcal{M} := L^2_0(\mathcal{B}, (\mathbb{R}^3)^1), \tag{39}$$

where

$$H_0(\mathrm{Div})^{(n)} := \left\{\boldsymbol{T} \in L^2\left(\mathcal{B}, (\mathbb{R}^d)^n\right) : \mathrm{Div}\, \boldsymbol{T} \in L^2\left(\mathcal{B}, (\mathbb{R}^d)^{n-1}\right) \text{ and } \boldsymbol{T}\boldsymbol{N}|_{\partial\mathcal{B}} = \boldsymbol{0}\right\}. \tag{40}$$

The small strain analogon to (22), (23), and (24) reads: Find $(\boldsymbol{H}, \boldsymbol{\Phi}, \boldsymbol{\mu}) \in \mathcal{V} \times \tilde{\mathcal{Q}} \times \mathcal{M}$ such that

$$\tilde{a}(\boldsymbol{H}, \delta\boldsymbol{H}) + b(\delta\boldsymbol{H}, \boldsymbol{\Phi}) = (\nabla \boldsymbol{g}, \delta\boldsymbol{H})_{L^2(\mathcal{B})},$$
$$b(\boldsymbol{H}, \delta\boldsymbol{\Phi}) + (\mathrm{Div}\, \delta\boldsymbol{\Phi}, \boldsymbol{\mu})_{L^2(\mathcal{B})} = 0,$$
$$(\delta\boldsymbol{\mu}, \mathrm{Div}\, \boldsymbol{\Phi})_{L^2(\mathcal{B})} = 0, \tag{41}$$

for all $(\delta\boldsymbol{H}, \delta\boldsymbol{\Phi}, \delta\boldsymbol{\mu}) \in \mathcal{V} \times \tilde{\mathcal{Q}} \times \mathcal{M}$.

Proposition 3. *Let* $\max\{\alpha, c_1\} > c > 0$ *and* $\max\{\alpha, c_1\} < C < \infty$. *There exists a unique solution to (41). Furthermore, if* $(\boldsymbol{H}, \boldsymbol{\Phi}, \boldsymbol{\mu}) \in \mathcal{V} \times \tilde{\mathcal{Q}} \times \mathcal{M}$ *is a solution to (41), then* $(\boldsymbol{H}, \boldsymbol{\Phi}) \in \mathcal{V} \times \mathcal{Q}$ *is a solution to (37). On the other hand, if* $(\boldsymbol{H}, \boldsymbol{\Phi}) \in \mathcal{V} \times \mathcal{Q}$ *is a solution to (37), then there exists* $\boldsymbol{\mu} \in \mathcal{M}$ *such that* $(\boldsymbol{H}, \boldsymbol{\Phi}, \boldsymbol{\mu}) \in \mathcal{V} \times \tilde{\mathcal{Q}} \times \mathcal{M}$ *is a solution to (41).*

The equivalence of Proposition 3 together with Proposition 2 implies that (17), (41), and (20) are equivalent to (33).

3.1.8 | Stability of the alternative 3D variational formulation

In the following we discuss the stability of the small strain analogon to the alternative 3D formulation (27) through (29). Let $H^{-1(n)}$ denote the dual space of $H_0^m(\mathcal{B};(\mathbb{R}^3)^n)$, that is, the space of all linear and continuous mappings from $H_0^m(\mathcal{B};(\mathbb{R}^3)^n)$ to $\mathbb{R}$ and define

$$H^{-1}(\mathrm{Div})^{(n)} := \{\boldsymbol{T} \in H^{-1(n)} : \mathrm{Div}\,\boldsymbol{T} \in H^{-1(n)}\}, \tag{42}$$

$$\hat{Q} := \{\boldsymbol{T} \in H^{-1}(\mathrm{Div})^{(n)} : \mathrm{Div}\,\boldsymbol{T} = 0\}. \tag{43}$$

Further, define the norm

$$\|\delta\boldsymbol{\Lambda}_c\|_{\hat{Q}} := \sup_{\delta\boldsymbol{H}\in\mathcal{V}\setminus\{0\}} \frac{\langle\delta\boldsymbol{\Lambda}_c, \delta\boldsymbol{H}\rangle}{|||\delta\boldsymbol{H}|||},$$

with the duality pairing $\langle\bullet,\bullet\rangle : H^{-1(2)} \times H_0^m(\mathcal{B};(\mathbb{R}^3)^2) \to \mathbb{R}$. We consider the problem:

The small strain analogon to (27), (28), and (29) then reads: Find $(\boldsymbol{H}, \boldsymbol{\Lambda}_c) \in \mathcal{V} \times \hat{Q}$ such that

$$\begin{aligned} \tilde{a}(\boldsymbol{H}, \delta\boldsymbol{H}) + \langle\boldsymbol{\Lambda}_c, \delta\boldsymbol{H}\rangle &= (\nabla\boldsymbol{g}, \delta\boldsymbol{H})_{L^2(\mathcal{B})}, \\ \langle\delta\boldsymbol{\Lambda}_c, \boldsymbol{H}\rangle &= 0, \end{aligned} \tag{44}$$

for all $(\delta\boldsymbol{H}, \delta\boldsymbol{\Lambda}_c) \in \mathcal{V} \times \hat{Q}$.

The following proposition states, that problem (44) is well posed, meaning it has a unique solution, which coincides with the solution of the original problem.

Proposition 4. *There exists a unique solution to (44). Furthermore, problems (44) and (37) are equivalent in the following sense: If $(\boldsymbol{H}, \boldsymbol{\Phi}) \in \mathcal{V} \times \mathcal{Q}$ is a solution to (37), then there exists $\boldsymbol{\Lambda}_c \in \hat{Q}$ such that $(\boldsymbol{H}, \boldsymbol{\Lambda}_c) \in \mathcal{V} \times \hat{Q}$ is a solution to (44) and $b(\delta\boldsymbol{H}, \boldsymbol{\Phi}) = \langle\boldsymbol{\Lambda}_c, \delta\boldsymbol{H}\rangle$ for all $\delta\boldsymbol{H} \in \mathcal{V}$. If on the other hand $(\boldsymbol{H}, \boldsymbol{\Lambda}_c) \in \mathcal{V} \times \hat{Q}$ is a solution to (44), then there exists $\boldsymbol{\Phi} \in \mathcal{Q}$ such that $(\boldsymbol{H}, \boldsymbol{\Phi}) \in \mathcal{V} \times \mathcal{Q}$ is a solution to (37).*

3.2 | Finite element approximations

For the finite element discretization, a partition of $\mathcal{B}$ into a set of simplices $\mathcal{T} = \bigcup_e T_e$ is considered, where $\mathcal{F}$ is the set of corresponding element faces. By standard FE procedure, the solution variables and test functions of the continuous weak forms of Section 3.1 are replaced by piecewise polynomial functions, that are defined in the following subsections. Moreover, matrix vector representations corresponding to the discretized weak forms are given.

3.2.1 | Discretization of the pre- and postprocessing step

In the following, vectors containing nodal degrees of freedom corresponding to the pre- and postprocessing problem (17) and (20) are denoted by $\underline{\boldsymbol{d}}_u$ and $\underline{\boldsymbol{d}}_g$. We introduce the vector-matrix interpolation operators

$$\underline{\boldsymbol{u}}^h = \underline{\boldsymbol{N}}_u\underline{\boldsymbol{d}}_u, \qquad \delta\underline{\boldsymbol{u}}^h = \underline{\boldsymbol{N}}_u\delta\underline{\boldsymbol{d}}_u, \qquad \nabla\underline{\boldsymbol{u}}^h = \underline{\boldsymbol{B}}_u\underline{\boldsymbol{d}}_u, \qquad \nabla\delta\underline{\boldsymbol{u}}^h = \underline{\boldsymbol{B}}_u\delta\underline{\boldsymbol{d}}_u, \tag{45}$$

$$\underline{\boldsymbol{g}}^h = \underline{\boldsymbol{N}}_u\underline{\boldsymbol{d}}_g, \qquad \delta\underline{\boldsymbol{g}}^h = \underline{\boldsymbol{N}}_u\delta\underline{\boldsymbol{d}}_g, \qquad \nabla\underline{\boldsymbol{g}}^h = \underline{\boldsymbol{B}}_u\underline{\boldsymbol{d}}_g, \qquad \nabla\delta\underline{\boldsymbol{g}}^h = \underline{\boldsymbol{B}}_u\delta\underline{\boldsymbol{d}}_g, \tag{46}$$

where $\underline{\boldsymbol{N}}_u$ and $\underline{\boldsymbol{B}}_u$ represent suitable finite element interpolation matrices containing Lagrange shape functions and corresponding derivatives (cf. Appendix A1). Inserting (45) and (46) and reformulating (17) and (20) leads to the following matrix equations

$$\delta_{\boldsymbol{u}} \Pi^h = \sum_{T\in\mathcal{T}} \delta\underline{\boldsymbol{d}}_u^T \Bigg(\underbrace{\int_T \underline{\boldsymbol{B}}_u^T \underline{\boldsymbol{B}}_u \, \mathrm{d}V}_{\underline{\boldsymbol{k}}_u} \underline{\boldsymbol{d}}_g - \underbrace{\int_T \underline{\boldsymbol{N}}_u^T \underline{\boldsymbol{f}} \, \mathrm{d}V - \int_{\delta T} \underline{\boldsymbol{N}}_u^T \underline{\boldsymbol{t}} \, \mathrm{d}A}_{\underline{\boldsymbol{r}}_u^{\mathrm{ext}}} \Bigg) = 0, \tag{47}$$

$$\delta_{\boldsymbol{g}} \Pi^h = \sum_{T\in\mathcal{T}} \delta\underline{\boldsymbol{d}}_g^T \Bigg(\underbrace{\int_T \underline{\boldsymbol{B}}_u^T \underline{\boldsymbol{B}}_u \, \mathrm{d}V}_{\underline{\boldsymbol{k}}_u} \underline{\boldsymbol{d}}_u - \underbrace{\int_T \underline{\boldsymbol{B}}_u^T \underline{\boldsymbol{N}}_H \underline{\boldsymbol{d}}_{H,\mathrm{ext}} \, \mathrm{d}V}_{\underline{\boldsymbol{r}}_H^{\mathrm{ext}}} \Bigg) = 0, \tag{48}$$

where $\underline{\boldsymbol{d}}_{H,\mathrm{ext}}$ contains the nodal degrees of freedom corresponding to $\underline{\boldsymbol{H}}^h$ computed by the main step. Note, that the pre- and postprocessing steps are linear and thus, even in the finite deformation regime, no further linearization of (47) and (48) is necessary.

3.2.2 | Discretization of the main step in 2D

For the discretization of the weak form (18), the following matrix interpolation operators are introduced (cf. Appendix A1):

$$\begin{aligned} \underline{\boldsymbol{H}}^h &= \underline{\boldsymbol{N}}_H \underline{\boldsymbol{d}}_H, & \nabla\underline{\boldsymbol{H}}^h &= \underline{\boldsymbol{B}}_H \underline{\boldsymbol{d}}_H, & \mathrm{Rot}\, \underline{\boldsymbol{H}}^h &= \underline{\boldsymbol{R}}_H \underline{\boldsymbol{d}}_H, \\ \delta\underline{\boldsymbol{H}}^h &= \underline{\boldsymbol{N}}_H \delta\underline{\boldsymbol{d}}_H, & \nabla\delta\underline{\boldsymbol{H}}^h &= \underline{\boldsymbol{B}}_H \delta\underline{\boldsymbol{d}}_H, & \mathrm{Rot}\, \delta\underline{\boldsymbol{H}}^h &= \underline{\boldsymbol{R}}_H \delta\underline{\boldsymbol{d}}_H. \end{aligned} \tag{49}$$

Since the solution variable $\boldsymbol{H}$ is sought in the $H^{1(2)}$ Sobolev space, Lagrange interpolation functions are used in matrices $\underline{\boldsymbol{N}}_H$ and $\underline{\boldsymbol{B}}_H$. The rotation operator matrix $\underline{\boldsymbol{R}}_H$ is constructed from the suitable components of the gradient operator with relation (16) (cf. Appendix A1). In the 2D case the Lagrange multiplier $\boldsymbol{\Phi} \in L^2$ is discretized with interpolation functions as

$$\underline{\boldsymbol{\Phi}}^h = \underline{\boldsymbol{N}}_\Phi \underline{\boldsymbol{d}}_\Phi \quad \text{and} \quad \delta\underline{\boldsymbol{\Phi}}^h = \underline{\boldsymbol{N}}_\Phi \delta\underline{\boldsymbol{d}}_\Phi. \tag{50}$$

As discussed in the mathematical stability analysis of Section 3.2.5 in 2D, any pairing of interpolation functions, which is stable for the Stokes problem (cf. Reference 24) is a suitable choice for the approximations $\underline{\boldsymbol{H}}^h$ and $\underline{\boldsymbol{\Phi}}^h$. Therefore, the Mini interpolation scheme P1B$_{\boldsymbol{H}}$-P1$_{\boldsymbol{\Phi}}$ and the Taylor–Hood interpolation schemes P2$_{\boldsymbol{H}}$-P1$_{\boldsymbol{\Phi}}$ and P3$_{\boldsymbol{H}}$-P2$_{\boldsymbol{\Phi}}$ are used (cf. overview in Table 1). Note, that in the Mini interpolation scheme $\underline{\boldsymbol{N}}_H$ consists of linear Lagrange shape functions corresponding to the vertex nodes of the (linear) P_1-triangle and the cubic Lagrange shape function corresponding to the interior node of the (cubic) P_3-triangular element. In this context the latter is also referred to as volume bubble function (cf. Section 3.2.5, see also Reference 25). The discretization of (49) and (50) reads

$$\delta_{\boldsymbol{H}} \Pi^h = \sum_{T\in\mathcal{T}} \delta\underline{\boldsymbol{d}}_H^T \Bigg(\underbrace{\int_T \frac{\partial \psi(\underline{\boldsymbol{d}}_H)}{\partial \underline{\boldsymbol{d}}_H} + \alpha \underline{\boldsymbol{R}}_H^T \underline{\boldsymbol{R}}_H \underline{\boldsymbol{d}}_H \mathrm{d}V}_{\underline{\boldsymbol{r}}_H(\underline{\boldsymbol{d}}_H)} + \underbrace{\int_T \underline{\boldsymbol{R}}_H^T \underline{\boldsymbol{N}}_\Phi \, \mathrm{d}V}_{\underline{\boldsymbol{k}}_{H\Phi}} \underline{\boldsymbol{d}}_\Phi - \underbrace{\int_T \underline{\boldsymbol{N}}_H^T \underline{\boldsymbol{B}}_u \underline{\boldsymbol{d}}_{g,\mathrm{ext}} \, \mathrm{d}V}_{\underline{\boldsymbol{r}}_g^{\mathrm{ext}}} \Bigg), \tag{51}$$

$$\delta_{\boldsymbol{\Phi}} \Pi^h = \sum_{T\in\mathcal{T}} \delta\underline{\boldsymbol{d}}_\Phi^T \Bigg(\underbrace{\int_T \underline{\boldsymbol{N}}_\Phi^T \underline{\boldsymbol{R}}_H \, \mathrm{d}V}_{\underline{\boldsymbol{k}}_{\Phi H}} \underline{\boldsymbol{d}}_H \Bigg). \tag{52}$$

TABLE 1 Overview of the two-dimensional finite element interpolation schemes used. For each scheme, the number of interpolation nodes is given in parantheses. The pre- and postprocessing elements are denoted by $P2_{\underline{g},\underline{u}}$, $P3_{\underline{g},\underline{u}}$, and $P4_{\underline{g},\underline{u}}$. The order of this listing corresponds to the order of the elements appearing in the table

Element name	$\underline{H}^h$	$\underline{\Phi}^h$	$\underline{g}^h/\underline{u}^h$
$P1B_{\underline{H}}$-$P1_{\underline{\Phi}}$ (MINI)	Linear (vertex), cubic (intern.) (4)	Linear (3)	Quadratic (6)
$P2_{\underline{H}}$-$P1_{\underline{\Phi}}$ (Taylor–Hood)	Quadratic (6)	Linear (3)	Cubic (10)
$P3_{\underline{H}}$-$P2_{\underline{\Phi}}$ (Taylor–Hood)	Cubic (10)	Quadratic (6)	Quadratic (15)

Here, $\underline{\boldsymbol{k}}_{H\Phi} = \underline{\boldsymbol{k}}_{\Phi H}^T$ represent the element submatrices corresponding to the rot-free constraint condition, whereas $\underline{\boldsymbol{r}}_g^{\text{ext}}$ depicts the nodal load vector with $\underline{\boldsymbol{d}}_{g,\text{ext}}$ obtained from the solution of the preprocessing step (47). In general, the strain energy function ψ is non-linear in $\underline{\boldsymbol{H}}^h$ and $\nabla\underline{\boldsymbol{H}}^h$ and thus, nonlinear in $\underline{\boldsymbol{d}}_H$. Therefore, the incremental Newton–Raphson loadstep solution procedure is used to obtain the solution. This requires the linearization of (51). The linearized problem then reads

$$\text{Lin}[\delta_{\boldsymbol{H}}\Pi^h + \delta_{\boldsymbol{\Phi}}\Pi^h] = \sum_{T\in\mathcal{T}} \begin{bmatrix}\delta\underline{\boldsymbol{d}}_H\\ \delta\underline{\boldsymbol{d}}_\Phi\end{bmatrix}^T \left(\begin{bmatrix}\underline{\boldsymbol{k}}_H & \underline{\boldsymbol{k}}_{H\Phi}\\ \underline{\boldsymbol{k}}_{\Phi H} & 0\end{bmatrix} \begin{bmatrix}\Delta\underline{\boldsymbol{d}}_H\\ \Delta\underline{\boldsymbol{d}}_\Phi\end{bmatrix} + \begin{bmatrix}\underline{\boldsymbol{r}}_H(\bar{\underline{\boldsymbol{d}}}_H) + \underline{\boldsymbol{r}}_g^{\text{ext}}\\ 0\end{bmatrix} \right) = 0, \tag{53}$$

where $\Delta\underline{\boldsymbol{d}}_H$ and $\Delta\underline{\boldsymbol{d}}_\Phi$ denote increments of the nodal solution vectors, and $\bar{\underline{\boldsymbol{d}}}_H$ denotes the nodal solution from the previous step. The element tangent submatrix $\underline{\boldsymbol{k}}_H$ can be written as

$$\underline{\boldsymbol{k}}_H = \frac{\partial \underline{\boldsymbol{r}}_H(\underline{\boldsymbol{d}}_H)}{\partial \underline{\boldsymbol{d}}_H} = \int_T \left(\frac{\partial^2 \psi(\underline{\boldsymbol{d}}_H)}{\partial \underline{\boldsymbol{d}}_H^2} + \alpha \underline{\boldsymbol{R}}_H^T \underline{\boldsymbol{R}}_H \right) \mathrm{d}V, \tag{54}$$

where the second term consists of the discretization of the rot–rot stabilization term. The integrals $\int_T \bullet\, \mathrm{d}V$ over the element are evaluated numerically via Gauss quadrature of the reference element.

3.2.3 | Discretization of the main step in 3D

In order to arrive at a stable discrete set of equations, in the 3D case the Lagrange multiplier is discretized conforming to the Sobolev space $H(\text{Div})$ (cf. Section 3.1.6). Therefore, the lowest order Raviart–Thomas interpolation procedure is used for $\underline{\boldsymbol{\Phi}}^h$. By using appropriate interpolation operator matrices, we denote the approximations as

$$\begin{aligned} \underline{\boldsymbol{\Phi}}^h &= \underline{\boldsymbol{S}}_\Phi \underline{\boldsymbol{d}}_\Phi, & \text{Div}\, \underline{\boldsymbol{\Phi}}^h &= \underline{\boldsymbol{D}}_\Phi \underline{\boldsymbol{d}}_\Phi,\\ \delta\underline{\boldsymbol{\Phi}}^h &= \underline{\boldsymbol{S}}_\Phi \delta\underline{\boldsymbol{d}}_\Phi, & \text{Div}\, \delta\underline{\boldsymbol{\Phi}}^h &= \underline{\boldsymbol{D}}_\Phi \delta\underline{\boldsymbol{d}}_\Phi, \end{aligned} \tag{55}$$

where $\underline{\boldsymbol{S}}_\Phi$ and $\underline{\boldsymbol{D}}_\Phi$ contain the Raviart–Thomas shape functions and their divergence, respectively. Details on the construction of $\underline{\boldsymbol{S}}_\Phi$ and $\underline{\boldsymbol{D}}_\Phi$ can be found in Appendix A1. Since the second Lagrange multiplier $\underline{\boldsymbol{\mu}}^h$ appearing in (23) and (24) is sought in L^2, a piecewise constant approximation is used. We define the interpolation matrix $\underline{\boldsymbol{N}}_\mu$ (cf. Appendix A1) with

$$\underline{\boldsymbol{\mu}}^h = \underline{\boldsymbol{N}}_\mu \underline{\boldsymbol{d}}_\mu \quad \text{and} \quad \delta\underline{\boldsymbol{\mu}}^h = \underline{\boldsymbol{N}}_\mu \delta\underline{\boldsymbol{d}}_\mu. \tag{56}$$

Note, that since $\underline{\boldsymbol{\mu}}^h$ is piecewise constant, the corresponding degrees of freedom $\underline{\boldsymbol{d}}_\mu$ may be condensed at the element level. An overview of the used Lagrange- and Raviart–Thomas interpolation schemes that fulfill the mathematical stability analysis of Section 3.2.5 can be found in Table 2. Here, for the interpolation of $\underline{\boldsymbol{H}}^h$, the matrix $\underline{\boldsymbol{N}}_H$ consists of the linear Lagrange shape functions corresponding to the four vertex nodes of the (linear) P_1-tetrahedron and the cubic Lagrange shape functions corresponding to the four midface nodes of the (cubic) P_3-tetrahedral element. In the mathematical analysis of Section 3.2.5, the latter are referred to as face bubble functions (see also Reference 19). Analogously to the

Variable name	Interpolation scheme	Interpolation type
$\underline{\boldsymbol{H}}^h$	Linear (vertex), cubic (midface) (8)	Lagrange
$\underline{\boldsymbol{\Phi}}^h/\underline{\boldsymbol{\Lambda}}_c^h$	Linear in face normal direction (midface) (4)	Raviart–Thomas
$\underline{\boldsymbol{\mu}}^h$	Constant (internal node) (1)	Piecewise constant
$\underline{\boldsymbol{u}}^h/\underline{\boldsymbol{g}}^h$	Quadratic (10)	Lagrange

TABLE 2 Overview of the three-dimensional finite element interpolation schemes (P1FB$_{\boldsymbol{H}}$-RT0$_{\boldsymbol{\Phi}}$-P0$_{\mu}$ and P1FB$_{\boldsymbol{H}}$-RT0$_{\boldsymbol{\Lambda}}$-P0$_{\mu}$). For each scheme, the number of interpolation nodes is given in parantheses. The pre- and postprocessing elements are denoted by $P2_{\boldsymbol{g},\boldsymbol{u}}$

discretization procedure discussed in the previous section, with (49), (55), and (56) we arrive at the following linearized system corresponding to the discretization of (22) through (24)

$$\mathrm{Lin}\left[\delta_{\boldsymbol{H}}\Pi^h + \delta_{\boldsymbol{\Phi}}\Pi^h\right] = \sum_{T\in\mathcal{T}} \begin{bmatrix} \delta\underline{\boldsymbol{d}}_H \\ \delta\underline{\boldsymbol{d}}_\Phi \\ \delta\underline{\boldsymbol{d}}_\mu \end{bmatrix}^T \left(\begin{bmatrix} \underline{\boldsymbol{k}}_H & \underline{\boldsymbol{k}}_{H\Phi} & 0 \\ \underline{\boldsymbol{k}}_{\Phi H} & 0 & \underline{\boldsymbol{k}}_{\Phi\mu} \\ 0 & \underline{\boldsymbol{k}}_{\mu\Phi} & 0 \end{bmatrix} \begin{bmatrix} \Delta\underline{\boldsymbol{d}}_H \\ \Delta\underline{\boldsymbol{d}}_\Phi \\ \Delta\underline{\boldsymbol{d}}_\mu \end{bmatrix} + \begin{bmatrix} \underline{\boldsymbol{r}}_H(\overline{\underline{\boldsymbol{d}}}_H) + \underline{\boldsymbol{r}}_g^{\mathrm{ext}} \\ 0 \\ 0 \end{bmatrix} \right) = 0. \tag{57}$$

The element tangent submatrices $\underline{\boldsymbol{k}}_{\Phi\mu} = \underline{\boldsymbol{k}}_{\mu\Phi}^T$ and $\underline{\boldsymbol{k}}_{H\Phi} = \underline{\boldsymbol{k}}_{\Phi H}^T$, which correspond to the rot-constraint and the div-constraint, respectively, are given by

$$\underline{\boldsymbol{k}}_{\Phi\mu} = \underline{\boldsymbol{k}}_{\mu\Phi}^T = \int_T \underline{\boldsymbol{D}}_\Phi^T \underline{\boldsymbol{N}}_\mu \,\mathrm{d}V, \tag{58}$$

$$\underline{\boldsymbol{k}}_{H\Phi} = \underline{\boldsymbol{k}}_{\Phi H}^T = \int_T \underline{\boldsymbol{R}}_H^T \underline{\boldsymbol{S}}_\Phi \,\mathrm{d}V. \tag{59}$$

In the following, the discretization scheme (57) is denoted by P1FB$_{\boldsymbol{H}}$-RT0$_{\boldsymbol{\Phi}}$-P0$_{\mu}$.

Remark 4. In Reference 19, for a similar discretization the approach following Reference 26 is taken in which the first Lagrange multiplier $\boldsymbol{\Phi}$ is discretized with P_0 functions. In a second constraint condition, added to the discrete system of equations, through discrete Lagrange multipliers $\boldsymbol{\gamma}^h$ continuity of $\boldsymbol{\Phi}$ in normal direction across the element faces is enforced. While this second constraint is not part of the continuous formulation, the global number of equations is similar to those of the proposed approach. For $d = 3$ the Lagrange multiplier and the additional constraint equation of one element contribute $\mathrm{ndof}_{\boldsymbol{\Phi}} + \mathrm{ndof}_{\boldsymbol{\gamma}^h} = 9 + 3 \cdot 4 = 21$ equations to the global system, where $\mathrm{ndof}_{\boldsymbol{\Phi}}$ may be condensed at the element level. Meanwhile, the P1FB$_{\boldsymbol{H}}$-RT0$_{\boldsymbol{\Phi}}$-P0$_{\boldsymbol{\mu}}$-element counts $\mathrm{ndof}_{\boldsymbol{\Phi}} + \mathrm{ndof}_{\boldsymbol{\mu}} = 3 \cdot 4 + 3 = 15$ corresponding degrees of freedom, where $\mathrm{ndof}_{\boldsymbol{\mu}}$ may be condensed at the element level.

3.2.4 | 3D discretization of the alternative formulation

For the discretization of the alternative approach (27) through (29), the same interpolation operators as in the previous section are used. Thus, the interpolation of $\boldsymbol{\Lambda}_c$ is given by

$$\begin{aligned} \underline{\boldsymbol{\Lambda}}_c^h &= \underline{\boldsymbol{S}}_\Phi \underline{\boldsymbol{d}}_{\Lambda_c}, & \mathrm{Div}\,\underline{\boldsymbol{\Lambda}}_c^h &= \underline{\boldsymbol{D}}_\Phi \underline{\boldsymbol{d}}_{\Lambda_c}, \\ \delta\underline{\boldsymbol{\Lambda}}_c^h &= \underline{\boldsymbol{S}}_\Phi \delta\underline{\boldsymbol{d}}_{\Lambda_c}, & \mathrm{Div}\,\delta\underline{\boldsymbol{\Lambda}}_c^h &= \underline{\boldsymbol{D}}_\Phi \delta\underline{\boldsymbol{d}}_{\Lambda_c}. \end{aligned} \tag{60}$$

Consequently, the structure of the linearized system of the discretized equations of (27) through (29) is analogous to the one in the previous section:

$$\mathrm{Lin}\left[\delta_{\boldsymbol{H}}\Pi^h + \delta_{\boldsymbol{\Phi}}\Pi^h\right] = \sum_{T\in\mathcal{T}} \begin{bmatrix} \delta\underline{\boldsymbol{d}}_H \\ \delta\underline{\boldsymbol{d}}_{\Lambda_c} \\ \delta\underline{\boldsymbol{d}}_\mu \end{bmatrix}^T \left(\begin{bmatrix} \underline{\boldsymbol{k}}_H & \underline{\boldsymbol{k}}_{H\Lambda_c} & 0 \\ \underline{\boldsymbol{k}}_{\Lambda_c H} & 0 & \underline{\boldsymbol{k}}_{\Lambda_c\mu} \\ 0 & \underline{\boldsymbol{k}}_{\mu\Lambda_c} & 0 \end{bmatrix} \begin{bmatrix} \Delta\underline{\boldsymbol{d}}_H \\ \Delta\underline{\boldsymbol{d}}_{\Lambda_c} \\ \Delta\underline{\boldsymbol{d}}_\mu \end{bmatrix} + \begin{bmatrix} \underline{\boldsymbol{r}}_H(\overline{\underline{\boldsymbol{d}}}_H) + \underline{\boldsymbol{r}}_g^{\mathrm{ext}} \\ 0 \\ 0 \end{bmatrix} \right) = 0. \tag{61}$$

However, here the tangent submatrix corresponding to the rot-constraint takes the form

$$\underline{\boldsymbol{k}}_{H\Lambda_c} = \underline{\boldsymbol{k}}_{\Lambda_c H}^T = \int_T \underline{\boldsymbol{N}}_H^T \underline{\boldsymbol{S}}_\Phi \, \mathrm{d}V. \tag{62}$$

The submatrices $\underline{\boldsymbol{k}}_H$ and $\underline{\boldsymbol{k}}_{\Lambda_c\mu} = \underline{\boldsymbol{k}}_{\Phi_\mu}$ remain unchanged (cf. Section 3.2.3). In the following, the discretization scheme corresponding to (61) is denoted by P1FB$_{\boldsymbol{H}}$-RT0$_{\boldsymbol{\Lambda}}$-P0$_\mu$ (cf. Table 2).

3.2.5 | Mathematical analysis of the finite element approximations

In this section we discuss the stability of the finite element approximation schemes discussed in the previous sections. Proofs of the propositions and lemmas of this section are given in appendix B1.

3.2.6 | Stability of the 2D finite element approximations

Let $A \lesssim B$ abbreviate that there exists a generic constant $C < \infty$, that does not depend on the critical parameter like the mesh-size of a discretization or the parameter c_1 and α defined below, such that $A \leq CB$.

In the case $d = 2$, any finite element pairing that is stable for the Stokes equations is a suitable choice for the discretization of (18) and (19). This is proved in the following proposition.

Proposition 5. *Let $c_1 > 0$, $\max\{\alpha, c_1\} > c > 0$ and $\max\{\alpha, c_1\} < C < \infty$. If $\mathcal{V}^h \times Q^h$ is a stable finite element pair for the Stokes equations, then $\mathcal{V}^h \times \mathcal{Q}^h$ is a stable pairing for the discretization of (37) for $d = 2$. Therefore, there exists a unique solution $(\boldsymbol{H}^h, \boldsymbol{\Phi}^h) \in \mathcal{V}^h \times \mathcal{Q}^h$ of the discretization with*

$$\begin{aligned} &|||\boldsymbol{H} - \boldsymbol{H}^h||| + \|\boldsymbol{\Phi} - \boldsymbol{\Phi}^h\|_{L^2(\mathcal{B})} \\ &\quad\lesssim \inf_{(\delta\boldsymbol{H}^h, \delta\boldsymbol{\Phi}^h) \in \mathcal{V}^h \times \mathcal{Q}^h} |||\boldsymbol{H} - \delta\boldsymbol{H}^h||| + \|\boldsymbol{\Phi} - \delta\boldsymbol{\Phi}^h\|_{L^2(\mathcal{B})}, \end{aligned} \tag{63}$$

where $(\boldsymbol{H}, \boldsymbol{\Phi}) \in \mathcal{V} \times \mathcal{Q}$ is the solution to problem (37).

For a simplicial triangulation $\mathcal{T}$ of $\mathcal{B}$, we introduce the following notation for the space of tensorial piecewise polynomial functions of degree $\leq k$:

$$P_k^{(n)} := P_k\left(\mathcal{T}; (\mathbb{R}^d)^{(n)}\right). \tag{64}$$

If $\boldsymbol{T}$ is a vector ($n = 1$), the corresponding superscript index will be omitted. We denote the discrete spaces corresponding to the MINI element by

$$\mathcal{V}_{\mathrm{M}}^h := \mathcal{V} \cap P_1^{(2)} \oplus B_3(\mathcal{T}, \mathbb{R}^2)^{(2)}, \tag{65}$$

$$\mathcal{Q}_{\mathrm{M}}^h := \mathcal{Q} \cap P_1. \tag{66}$$

Here, $B_3(\mathcal{T}, \mathbb{R}^2)^{(2)}$ is the space of cubic bubble functions defined on the triangle (cf. Reference 25). The discretization of (37) then seeks $(\boldsymbol{H}^h, \boldsymbol{\Phi}^h) \in \mathcal{V}_{\mathrm{M}}^h \times \mathcal{Q}_{\mathrm{M}}^h$ such that (37) is solved for all test functions $(\delta\boldsymbol{H}^h, \delta\boldsymbol{\Phi}^h) \in \mathcal{V}_{\mathrm{M}}^h \times \mathcal{Q}_{\mathrm{M}}^h$. The inf-sup condition for the Stokes equations (Reference 24, theorem 8.8.1) together with Proposition 5 proves the stability of this discretization, and therefore, a unique solution exists and the error satisfies (63). The Taylor–Hood finite element subspaces (cf. Reference 25) are

$$\mathcal{V}_{\mathrm{TH}}^h := \mathcal{V} \cap P_{k+1}^{(2)} \quad \text{and} \quad \mathcal{Q}_{\mathrm{TH}}^h := \mathcal{Q} \cap P_k \ \text{ for } \ k \geq 1, \tag{67}$$

and the discrete problem seeks $(\boldsymbol{H}^h, \boldsymbol{\Phi}^h) \in \mathcal{V}_{\mathrm{TH}}^h \times \mathcal{Q}_{\mathrm{TH}}^h$ such that (37) is solved for all $(\delta\boldsymbol{H}^h, \delta\boldsymbol{\Phi}^h) \in \mathcal{V}_{\mathrm{TH}}^h \times \mathcal{Q}_{\mathrm{TH}}^h$. Again, the inf-sup condition for the Stokes equations[24] together with Proposition 5 proves that this defines a stable discretization. For $k = 1$ and $k = 2$, respectively, the corresponding finite elements are referred to by P2$_{\boldsymbol{H}}$-P1$_{\boldsymbol{\Phi}}$ and P3$_{\boldsymbol{H}}$-P2$_{\boldsymbol{\Phi}}$ in the following (Table 1).

3.2.7 | Stability of the 3D finite element approximations

As discussed in Section 3.1.6, for $d=3$ the Lagrange multiplier $\boldsymbol{\Phi} \in \mathcal{Q}$ is required to be divergence free. Thus, the formulation with an additional Lagrange multiplier from Section 3.1.4 is employed with the following discrete subspaces:

$$\mathcal{V}^h := \mathcal{V} \cap P_1^{(2)} \oplus B_3(\mathcal{F}, \mathbb{R}^3)^{(2)}, \tag{68}$$

$$\mathcal{Q}^h := \tilde{\mathcal{Q}} \cap RT_0(\mathcal{T}; \mathbb{R}^3)^{(2)} \text{ and} \tag{69}$$

$$\mathcal{M}^h := \mathcal{M} \cap P_0. \tag{70}$$

Here, $B_3(\mathcal{F}, \mathbb{R}^3)$ denotes the space of cubic face bubble functions vanishing on the element edges. Furthermore, $RT_0(\mathcal{T}; \mathbb{R}^3)$ is the finite element space of Raviart and Thomas, which consists of polynomial functions, which are continuous in normal direction across the interelement boundarys.[27] The discretization of the modified problem (41) seeks $(\boldsymbol{H}^h, \boldsymbol{\Phi}^h, \boldsymbol{\mu}^h) \in \mathcal{V}^h \times \mathcal{Q}^h \times \mathcal{M}^h$ such that (41) is solved for all test functions $(\delta\boldsymbol{H}^h, \delta\boldsymbol{\Phi}^h, \delta\boldsymbol{\mu}^h) \in \mathcal{V}^h \times \mathcal{Q}^h \times \mathcal{M}^h$. This linear problem corresponds to the P1FB$_{\boldsymbol{H}}$-RT0$_{\boldsymbol{\Phi}}$-P0$_{\boldsymbol{\mu}}$ discretization of Section 3.2.3.

The following proposition proves the stability and an error estimate for this discretization.

Proposition 6. *Let $c_1 > 0$, $\max\{\alpha, c_1\} > c > 0$ and $\max\{\alpha, c_1\} < C < \infty$. The discretization of (41) with the above choice of spaces has a unique solution $(\boldsymbol{H}^h, \boldsymbol{\Phi}^h, \boldsymbol{\mu}^h) \in \mathcal{V}^h \times \mathcal{Q}^h \times \mathcal{M}^h$ satisfying*

$$\begin{aligned} &|||\boldsymbol{H} - \boldsymbol{H}^h||| + \|\boldsymbol{\Phi} - \boldsymbol{\Phi}^h\|_{L^2(\mathcal{B})} \\ &\quad \lesssim \inf_{(\delta\boldsymbol{H}^h, \delta\boldsymbol{\Phi}^h) \in \mathcal{V}^h \times (\mathcal{Q}^h \cap \mathcal{Q})} |||\boldsymbol{H} - \delta\boldsymbol{H}^h||| + \|\boldsymbol{\Phi} - \delta\boldsymbol{\Phi}^h\|_{L^2(\mathcal{B})}, \end{aligned}$$

where $(\boldsymbol{H}, \boldsymbol{\Phi}) \in \mathcal{V} \times \mathcal{Q}$ is the solution to (37).

3.2.8 | Stability of the alternative 3D finite element approximation

This section investigates a discretization of the alternative formulation (44), which is the linear analogon to (27) through (29), which showed appropriate performance in the numerical experiments.

The space $\hat{\mathcal{Q}}$ in (44) is discretized with $\hat{\mathcal{Q}} \cap \hat{\mathcal{Q}}^h$ with $\hat{\mathcal{Q}}^h := RT_0(\mathcal{T}; \mathbb{R}^3)^{(2)} \cap H(\mathrm{Div})^{(2)}$. In particular, those functions have more smoothness than requested by $\hat{\mathcal{Q}}$, namely they are in $H(\mathrm{Div})^{(2)}$. Therefore, the duality pairing can be replaced by the L^2 product. Moreover, since $\mathrm{Div}\, \hat{\mathcal{Q}}^h \subseteq P_0$, the equation $(\delta\boldsymbol{\mu}^h, \mathrm{Div}\, \boldsymbol{\Lambda}_{\mathrm{c}}^h)_{L^2(\mathcal{B})} = 0$ for all $\delta\boldsymbol{\mu}^h \in P_0$ guarantees that a function $\boldsymbol{\Lambda}_{\mathrm{c}}^h \in \hat{\mathcal{Q}}^h$ is in fact in $\hat{\mathcal{Q}}$. Thus, the divergence free condition from $\hat{\mathcal{Q}}$ can be incorporated via an additional Lagrange multiplier. In conclusion, the discrete problem for (44) seeks $(\boldsymbol{H}^h, \boldsymbol{\Lambda}_{\mathrm{c}}^h, \boldsymbol{\mu}^h) \in \mathcal{V}^h \times \hat{\mathcal{Q}}^h \times \hat{\mathcal{M}}^h$ so that

$$\begin{aligned} \tilde{a}(\delta\boldsymbol{H}^h, \boldsymbol{H}^h) + \left(\delta\boldsymbol{H}^h, \boldsymbol{\Lambda}_{\mathrm{c}}^h\right)_{L^2(\mathcal{B})} &= \left(\delta\boldsymbol{H}^h, \nabla\boldsymbol{g}^h\right)_{L^2(\mathcal{B})}, \\ \left(\delta\boldsymbol{\Lambda}_{\mathrm{c}}^h, \boldsymbol{H}^h\right)_{L^2(\mathcal{B})} + \left(\mathrm{Div}\, \delta\boldsymbol{\Lambda}_{\mathrm{c}}^h, \boldsymbol{\mu}^h\right)_{L^2(\mathcal{B})} &= 0, \\ \left(\delta\boldsymbol{\mu}^h, \mathrm{Div}\, \boldsymbol{\Lambda}_{\mathrm{c}}^h\right)_{L^2(\mathcal{B})} &= 0, \end{aligned} \tag{71}$$

for all $(\delta\boldsymbol{H}^h, \delta\boldsymbol{\Lambda}_{\mathrm{c}}^h, \delta\boldsymbol{\mu}^h) \in \mathcal{V}^h \times \hat{\mathcal{Q}}^h \times \hat{\mathcal{M}}^h$ with the modified discrete subspaces

$$\hat{\mathcal{Q}}^h := H(\mathrm{Div})^{(2)} \cap RT_0(\mathcal{T}; \mathbb{R}^3)^{(2)} \text{ and} \tag{72}$$

$$\hat{\mathcal{M}}^h := L^2(\mathcal{B}, (\mathbb{R}^3)^1) \cap P_0 \tag{73}$$

and $\mathcal{V}^h$ from (68) from the previous section.The discretization of (71) corresponds to the P1FB$_{\boldsymbol{H}}$-RT0$_{\boldsymbol{\Lambda}}$-P0$_{\boldsymbol{\mu}}$ formulation of Section 3.2.4. Note that $\boldsymbol{\mu}^h$ can be both identified as Lagrange multiplier enforcing $\boldsymbol{\Lambda}_{\mathrm{c}}^h$ to be divergence free and P_0 approximation of the displacement.

As mentioned above, since $\mathrm{Div}\, \hat{\mathcal{Q}}^h \subseteq P_0$, the third equation of (71) shows that $\boldsymbol{\Lambda}_{\mathrm{c}}^h \in \hat{\mathcal{Q}}^h \cap \hat{\mathcal{Q}}$. Therefore, the discretization (71) is a conforming discretization of (44) in the space $\mathcal{V}^h \times (\hat{\mathcal{Q}}^h \cap \hat{\mathcal{Q}}) \subseteq \mathcal{V} \times \hat{\mathcal{Q}}$. Proposition 4 proves the well-posedness of problem (44). Furthermore, the discretized problem is stable in the numerical experiments of section 4.

4 | NUMERICAL TESTS

In this section, the proposed discretizations are numerically tested. An overview of the considered elements is given in Table 3. For the implementation, the AceGen/AceFEM software package has been used, which is based on automatic differentiation. Through construction of the elastic potential containing the approximated solution fields and differentiation with respect to the nodal degrees of freedom on the element level, both the element residual and tangent matrix are derived (cf. Reference 28). The integrals are evaluated numerically with Gauss integration over the corresponding reference coordinate space. In Table 3 the used Gauss integration orders are shown for each discretization. The standard Newton–Raphson load step solution procedure is used for the solution of the nonlinear global system. For the solution of the linearized system of equations, the PARDISO solver is used.

For the local hyperelastic energy density the Neo Hookean ansatz of Reference 29 is used:

$$\psi^{\text{loc}} = \frac{\mu}{2}(I_1 - 3) + g(J), \tag{74}$$

$$\text{with} \quad g(J) = c(J^2 - 1) - d \ln J - \mu \ln J, \tag{75}$$

and $I_1 = \operatorname{tr} \boldsymbol{C}, J = \det \boldsymbol{F}$. The coefficients c and d are set to $c = \lambda/4$ and $d = \lambda/2$ (see also Reference 30), where the parameters λ and μ are the Lamé constants which can be computed from the Young's modulus E and the Poisson's ratio ν by $\lambda = E\nu/((1+\nu)(1-2\nu))$ and $\mu = E/(2(1+\nu))$. Based thereon, the Cauchy stress tensor can be computed from $\boldsymbol{\sigma} = J^{-1}\boldsymbol{P}\,\boldsymbol{F}^T$ where the first Piola–Kirchhoff stress tensor is obtained from $\boldsymbol{P} = \partial_F \psi$. The nonlocal part of the energy density is taken from:[31]

$$\psi^{\text{nloc}} = \frac{c_1}{2} \nabla \boldsymbol{F} \cdot \nabla \boldsymbol{F}, \tag{76}$$

where c_1 is a nonlocal elasticity constant. With $l = \sqrt{c_1/\mu}$, the constant can be scaled to a length unit parameter.[10] In the following numerical examples the elasticity parameters are chosen with $E = 500$ MPa and $\nu = 0.3$, unless stated otherwise. For the 2D analysis, the constitutive model is implemented under the plain strain assumption.

4.1 | Unit square with smooth solution

For this test, the domain $\mathcal{B}$ is considered to be a 2D unit square with the dimensions 1×1 mm^2 (cf. Figure 1(A)), where also the element alignment for the initial mesh is depicted. A cross-pattern element patch has been chosen, since a mesh with a unidirectional element orientation may show inferior convergence results (cf. Reference 32). In order to construct an exact error measure, the large displacement smooth reference solution $\boldsymbol{u}$ of Reference 18(p. 12) is used. The reference solution $\boldsymbol{u}|_{\partial\mathcal{B}} = \boldsymbol{0}$ and its first-order gradient $\nabla\boldsymbol{u}|_{\partial\mathcal{B}} = \boldsymbol{0}$ vanishes on the boundary, such that the strong form of (11) reads

$$-\operatorname{Div} \boldsymbol{P} + \operatorname{Div}\operatorname{Div} \boldsymbol{G} = \boldsymbol{f}. \tag{77}$$

TABLE 3 Overview of applied Gauss integration schemes. As introduced in Section 3.2 the indices in the element name refer to the approximated field. Furthermore, the following abbreviations for the different approximations hold: P(•): nodal interpolation with Lagrange polynomials of (•)th order (for (•) ≥ 1). P0, piecewise constant approximation; B, enrichment by volume bubble function; FB, enrichment by face bubble function; RT0, lowest-order Raviart–Thomas interpolation

Element name	Number of Gauss points	AceGen ID
$\text{P2}_{\boldsymbol{g},\boldsymbol{u}}$ (pre,post,2D)	3	35
$\text{P3}_{\boldsymbol{g},\boldsymbol{u}}$ (pre,post,2D)	7	42
$\text{P4}_{\boldsymbol{g},\boldsymbol{u}}$ (pre,post,2D)	12	39
$\text{P1B}_{\boldsymbol{H}}$-$\text{P1}_{\boldsymbol{\Phi}}$	3	35
$\text{P2}_{\boldsymbol{H}}$-$\text{P1}_{\boldsymbol{\Phi}}$	7	42
$\text{P3}_{\boldsymbol{H}}$-$\text{P2}_{\boldsymbol{\Phi}}$	12	39
$\text{P2}_{\boldsymbol{g}}$ (pre 3D)	4	18
$\text{P2}_{\boldsymbol{u}}$ (post 3D)	5	19
$\text{P1FB}_{\boldsymbol{H}}$-$\text{RT0}_{\boldsymbol{\Phi}}$-$\text{P0}_{\mu}$	4	18
$\text{P1FB}_{\boldsymbol{H}}$-$\text{RT0}_{\boldsymbol{\Lambda}}$-$\text{P0}_{\mu}$	4	18

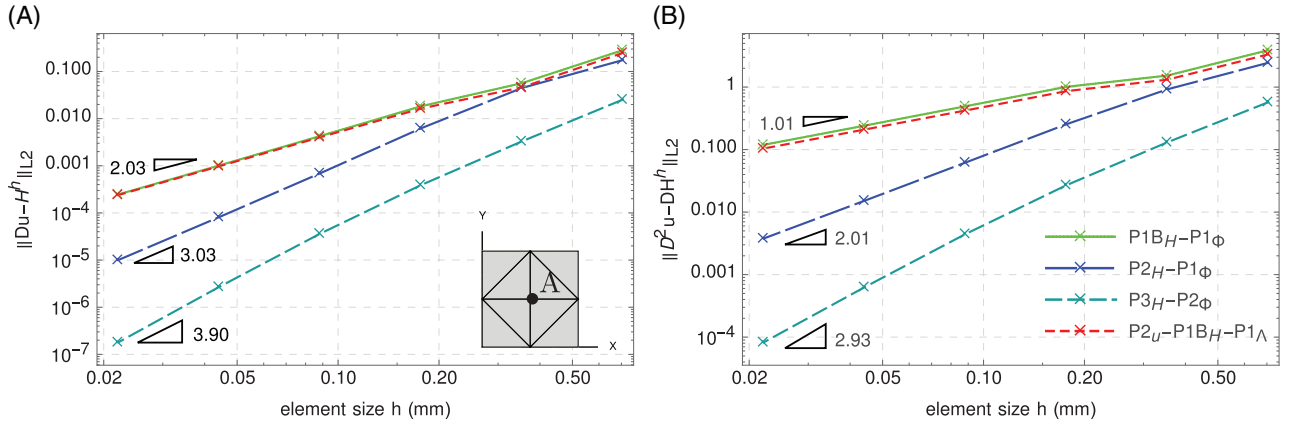

FIGURE 1 Convergence rates in the (A) H^1-error seminorm and in the (B) H^2-error seminorm of the proposed elements compared to the three field element P2$_{\boldsymbol{u}}$-P1B$_{\boldsymbol{H}}$-P1$_{\Lambda}$ of Reference 18. For this study the nonlocal parameter is set to $l = 0.1$ mm. In subfigure (A) the initial mesh is depicted

Element name	Pre- and postprocessing
P1B$_{\boldsymbol{H}}$-P1$_{\boldsymbol{\Phi}}$	P2$_{\boldsymbol{g,u}}$
P2$_{\boldsymbol{H}}$-P1$_{\boldsymbol{\Phi}}$	P3$_{\boldsymbol{g,u}}$
P3$_{\boldsymbol{H}}$-P2$_{\boldsymbol{\Phi}}$	P4$_{\boldsymbol{g,u}}$
P1FB$_{\boldsymbol{H}}$-RT0$_{\boldsymbol{\Phi}}$-P0$_{\mu}$	P2$_{\boldsymbol{g,u}}$
P1FB$_{\boldsymbol{H}}$-RT0$_{\boldsymbol{\Lambda}}$-P0$_{\mu}$	P2$_{\boldsymbol{g,u}}$

TABLE 4 Overview of the analyzed finite elements and associated pre- and postprocessing elements

With (77), the volume load $\boldsymbol{f}$ is computed analytically for each Gauss point and then evaluated through $\underline{\boldsymbol{r}}_u^{\text{ext}}$ of the discrete Equation (47). For each uniform mesh refinement step the error $\|\nabla \boldsymbol{u} - \boldsymbol{H}^h\|_{L^2(\mathcal{B})}$ and $\|\nabla^2 \boldsymbol{u} - \nabla \boldsymbol{H}^h\|_{L^2(\mathcal{B})}$ is measured by computing the numerical integrals, in which the exact solution and the interpolation of the finite element solution are evaluated at the Gauss points. The polynomial order of both pre- and postprocessing discretization is $k+1$, where k is the polynomial order of the $\boldsymbol{H}^h$ interpolation of the main step (cf. Table 4). The elements are compared to the P2$_{\boldsymbol{u}}$-P1B$_{\boldsymbol{H}}$-P1$_{\Lambda}$ element of.[18] There, following the previously existing mixed approaches (cf. References 16 and 17), the displacement gradient is replaced by $\boldsymbol{H}$ only in the nonlocal energy $\psi^{\text{nloc}} := \psi^{\text{nloc}}(\boldsymbol{H})$ and $\psi^{\text{loc}} := \psi^{\text{loc}}(\nabla \boldsymbol{u})$ remains a functional of $\boldsymbol{u}$. The discretization of the P2$_{\boldsymbol{u}}$-P1B$_{\boldsymbol{H}}$-P1$_{\Lambda}$ element is in accordance to the naming convention used here (cf. Table 3). Moreover, the Lagrange multiplier is not additively decomposed and sought in L^2. Therefore, the corresponding variational problem is not decoupled.

4.1.1 | Convergence rates

Figure 1 depicts the error in the H^1 and the H^2 seminorm depending on the element size h. For the convergence study the nonlocal parameter $l = 0.1$ mm is chosen and with $\alpha = 0$ the rot-rot stabilization term is switched off. The observed H^1 convergence rates are approximately h^{k+1} for the H^1 error and h^k for the H^2 error, where k is the polynomial order of $\boldsymbol{H}^h$. The L^2 norm $\|\text{Rot}\, \boldsymbol{H}^h\|_{L^2(\mathcal{B})}$ of the constraint term (cf. (52)) is observed to decrease with the same rate as the H^2-error.

4.1.2 | Influence of the stabilization term

For the results depicted in Figure 2(A), the rot-rot stabilization term is switched on with $\alpha = 10\ \text{N/mm}^3 L$. The convergence of the L^2 error corresponding to the P2$_{\boldsymbol{H}}$-P1$_{\boldsymbol{\Phi}}$ element is shown for various nonlocal parameters l. The approximate convergence rate of h^4 is obtained (for this element the pre- and postprocessing polynomial order is

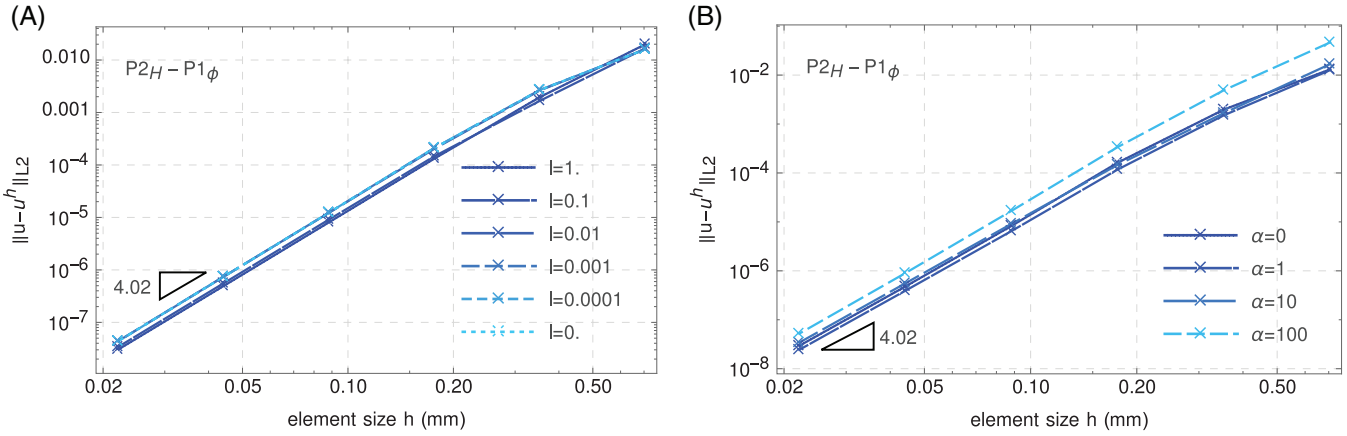

FIGURE 2 Influence of the stabilization parameter: L^2 convergence of the $\mathrm{P2}_{\boldsymbol{H}}$-$\mathrm{P1}_{\boldsymbol{\Phi}}$ Taylor–Hood-type element on the unit square problem (A) for varying l with the fixed stabilization parameter $\alpha = 10\mathrm{N/mm}^3 L$ and (B) for varying stabilization parameter α for a fixed length parameter $l = 0.1L$

cubic with $\boldsymbol{u}^h \in \mathcal{G}^h \cap P_3$, cf. Table 4). The convergence rate h^4 is reached even in the limit case of vanishing nonlocal contribution ($l = 0$). While the Taylor–Hood-type element $\mathrm{P3}_{\boldsymbol{H}}$-$\mathrm{P2}_{\boldsymbol{\Phi}}$ behaves analogously with an approximate L^2 convergence rate of h^5, the $\mathrm{P1B}_{\boldsymbol{H}}$-$\mathrm{P1}_{\boldsymbol{\Phi}}$ element experiences a shift from order h^3 to h^2 as l approaches zero. The tangent matrix of the element $\mathrm{P2}_{\boldsymbol{u}}$-$\mathrm{P1B}_{\boldsymbol{H}}$-$\mathrm{P1}_{\boldsymbol{\Lambda}}$ becomes singular in this case. In Figure 2(B) the convergence behavior of the $\mathrm{P2}_{\boldsymbol{H}}$-$\mathrm{P1}_{\boldsymbol{\Phi}}$ element depending on the numerical value of α is depicted. While it can be observed that numerical values up to $\alpha = 10\ \mathrm{N/mm}^3 L$ do not significantly alter the convergence behavior, a higher value than $\alpha = 10\ \mathrm{N/mm}^3 L$ leads to slightly varying results. This may be due to the fact that in this case the rot-free constraint is dominated more by the stabilization term, which for high values of α can be interpreted as penalty term. Moreover, for higher values of α an increase of the condition number of the global tangent matrix and, for more extreme values, loss of convergence of the Newton-Raphson solution procedure is observed.

4.1.3 | Computing efficiency

In order to compare the computational cost of the finite elements, Figure 3 shows a displacement convergence study at the point $A = (0.5, 0.5)$ mm. In Figure 3(A) the displacement of the finite element solution relative to the exact solution $u_y(0.5, 0.5) = -0.1953$ mm is plotted versus the computing time required for both assembly and solution of all iterative steps of the solution procedure in total at each refinement step. Since the scale of the problem is rather small, multiple simulations are made at each refinement step. The computing times of all simulations for each refinement step are averaged to take into account variations of the calculating capacity of the computer. Figure 3(B) depicts the average computing time of the elements corresponding to the converged state. The convergence criterion is $|\Delta \boldsymbol{u}| \leq 0.001$ mm and the corresponding refinement stage is marked by a bullet in Figure 3(A). While for all elements the computing time corresponding to the main problem (53) is considered, for element $\mathrm{P3}_{\boldsymbol{H}}$-$\mathrm{P2}_{\boldsymbol{\Phi}}$ the total computing time including pre- and postprocessing is additionally taken into account (the corresponding plot in Figure 3(B) is marked with an asterisk). It becomes evident, that even for this small-sized problem, the proposed elements have a computational advantage over the three-field element $\mathrm{P2}_{\boldsymbol{u}}$-$\mathrm{P1B}_{\boldsymbol{H}}$-$\mathrm{P1}_{\boldsymbol{\Lambda}}$. Moreover, the contribution of the pre- and postprocessing step to the total computing time is relatively small even in the present case of $\mathrm{P4}_{\boldsymbol{u},\boldsymbol{g}}$ elements (cf. Table 4).

4.2 | Cook's membrane problem

The boundary of the Cook's membrane problem (cf. Figure 4(A)) is decomposed with $\partial\mathcal{B} = \Gamma_D \cup \Gamma_N = \Gamma_M$. On the left side at ($X = 0$ mm) the Dirichlet boundary conditions $\boldsymbol{u}|_{\Gamma_D} = \boldsymbol{0}$ and $\boldsymbol{H} \wedge \boldsymbol{N}|_{\Gamma_D} = \boldsymbol{0}$ hold. On the right-hand side at ($X = L$, with $L = 48$ mm) the surface traction $\boldsymbol{t} = (0, 50\ \mathrm{N/mm})^T$ is applied. With $\partial\mathcal{B} = \Gamma_M$ and $\Gamma_H = \emptyset$ no higher-order Dirichlet

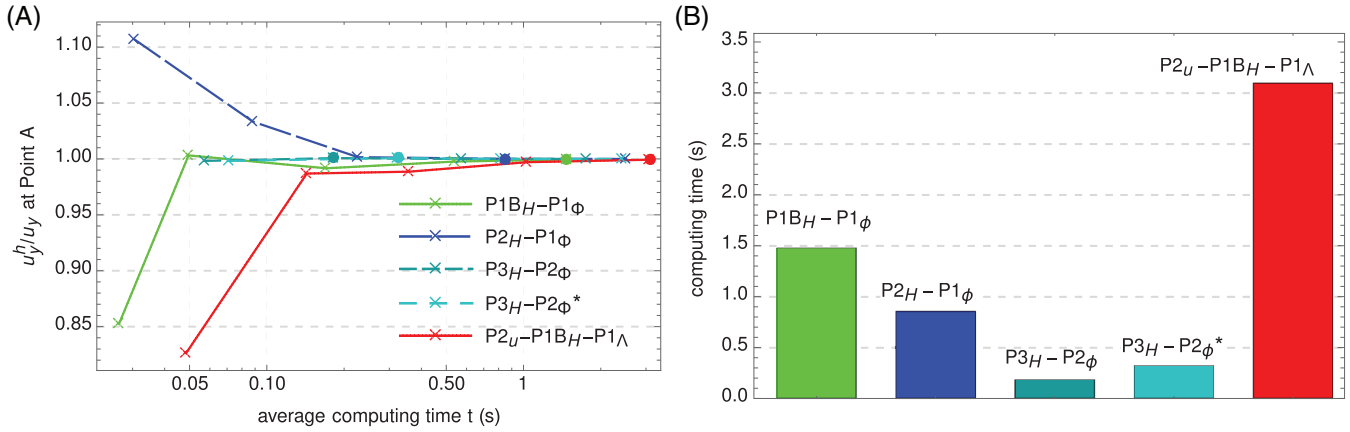

FIGURE 3 Computing efficiency: (A) displacements at center point A (cf. Figure 1(A)) normalized by reference value versus average computing time and (B) computing time corresponding to the converged state. Converged states are market by bullets in (A)

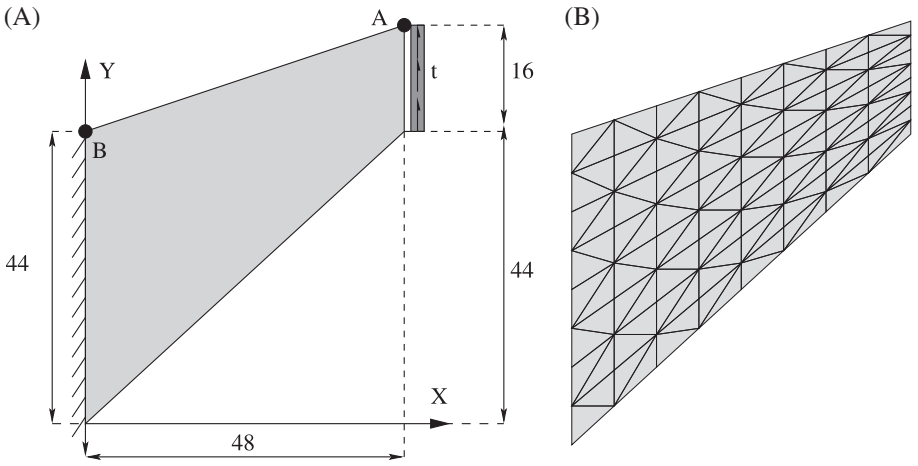

FIGURE 4 (A) Geometry of the Cook's membrane benchmark problem ([length] = mm) and distributed traction $t = 50.00$ N/mm. (B) Visualization of the mesh corresponding to the second refinement step

boundary conditions are prescribed. The nonlocal parameter is $l = 1$ mm and the stabilization parameter is $\alpha = 10\ L$. The mesh (cf. Figure 4) is refined uniformly. We denote

$$\langle \boldsymbol{\sigma} \rangle_e^2 = \frac{\|\boldsymbol{\sigma}^h\|^2_{L^2(\mathcal{B}_e)}}{V_e} \tag{78}$$

as the element average stress, where $\boldsymbol{\sigma}^h$ is the Cauchy Stress obtained by postprocessing of the finite element solution.

4.2.1 | Removal of singularities

In order to show the ability to avoid singularities, the gradient elasticity elements are compared to the quadratic local elasticity element P2$_{\boldsymbol{u}}$ (discretization of (11) with $\boldsymbol{G} = \boldsymbol{0}$ and $\boldsymbol{u}^h \in H^1_{\Gamma_D} \cap P_2$). For this, the average stress $\langle \boldsymbol{\sigma} \rangle_e$ of the element adjacent to the singularity point $B = (0, 44)$ mm is evaluated. In Figure 5, the element average stress is plotted versus the global number of degrees of freedom corresponding to each refinement step. It becomes evident, that for an increasing number of degrees of freedom, the element average stress of the gradient elasticity elements converges similarly toward a finite value, while the element average stress of the local P2$_{\boldsymbol{u}}$ element increases. This behavior is illustrated in Figure 6, in which contour plots of the average element stresses are shown for the sixth refinement step (cf. bullet marks in Figure 5). The enlarged image sections (Figure 6(C),(D)) reveal the strong stress localization of the local formulation compared to the proposed nonlocal P1B$_{\boldsymbol{H}}$-P1$_{\boldsymbol{\Phi}}$ element.

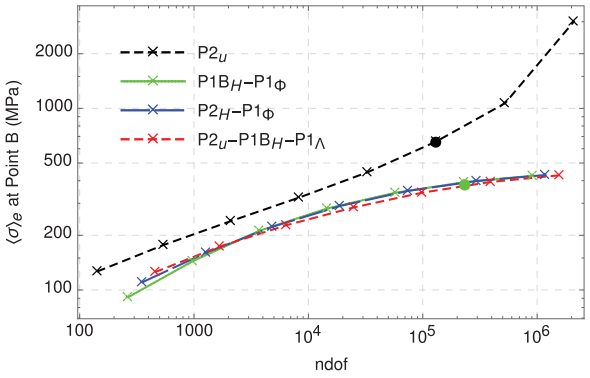

FIGURE 5 Uniform mesh refinement: average stress of the element closest to the singularity point B over global number of degrees of freedom

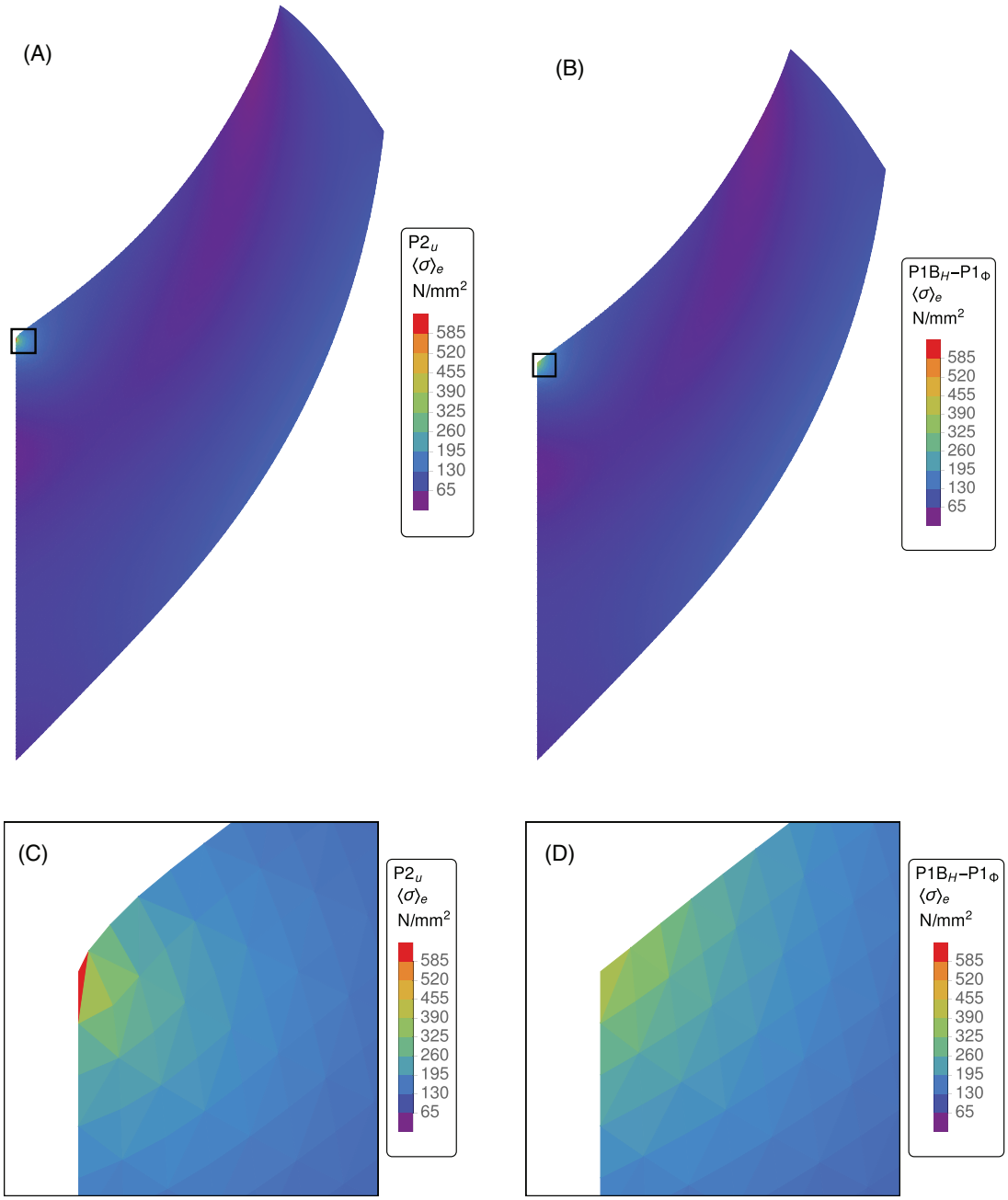

FIGURE 6 Nonsmoothed contour plots of the element average stress values $\langle\boldsymbol{\sigma}\rangle_e$ (A) for the $P_{\boldsymbol{u}}$ local displacement element and (B) for the proposed $P1B_{\boldsymbol{H}} - P1_{\boldsymbol{\Phi}}$ element. In (C) and (D) enlarged image sections around the stress localization point are shown: no stress singularity is observed for the nonlocal formulation

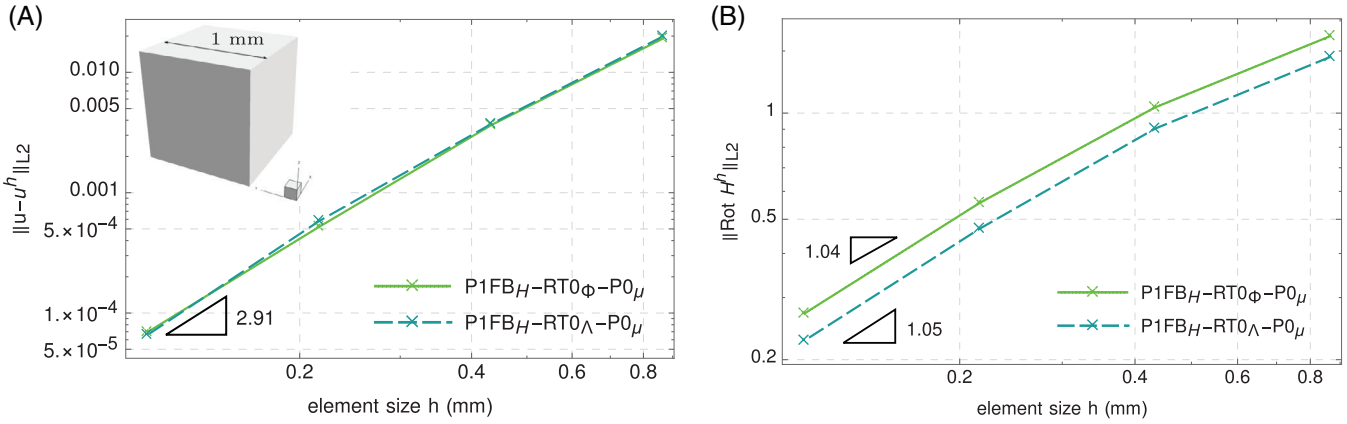

FIGURE 7 Convergence rates of the proposed elements in three-dimensional (cf. Table 3)(A) in the L^2-error and (B) in the L^2 norm $\|\mathrm{Rot}\,\boldsymbol{H}\|_{L^2(\mathcal{B})}$. For this study the parameter for the nonlocal energy is set to $l = 1$ mm

4.3 | 3D Unit cube with smooth solution

For the investigation of the convergence behavior of the 3D elements the unit square domain is extended to 3D. Here, $\mathcal{B}$ has the dimensions $1 \times 1 \times 1$ mm^3 (cf. Figure 7(A)). The smooth finite strain reference solution of Reference 18 (p. 14) is used and again, with the strong form (77) the right-hand side $\boldsymbol{f}$ is derived analytically. The convergence of the L^2-error is depicted in Figure 7(A). The nonlocal parameter is $l = 1$ mm and the rot-rot stabilization term is switched off with $\alpha = 0$. It is observed that both investigated elements converge similarly. From Figure 7(B) it can be seen, that for both elements the L^2-norm $|\,|\mathrm{Rot}\,\boldsymbol{H}|\,|_{L^2(\mathcal{B})}$ of the constraint condition decreases approximately with the order h.

4.4 | 3D Cook's problem

In this subsection the 3D Cook's problem (cf. Figure 8(A)) is considered. Similar to the 2D case of Section 4.2, the boundary is decomposed with $\partial\mathcal{B} = \Gamma_D \cup \Gamma_N = \Gamma_M$. The essential boundary condition at $X = 0$ mm reads $\boldsymbol{u}|_{\Gamma_D} = \boldsymbol{0}$ and $\boldsymbol{H} \wedge \boldsymbol{N}|_{\Gamma_D} = \boldsymbol{0}$. At $X = L = 48$ mm the surface load $\boldsymbol{t} = (0, 0, 50\ \mathrm{MPa})$ is applied.

4.4.1 | Influence of the nonlocal parameter on the displacement response

For a mesh refinement stage corresponding to 5120 elements (cf. Figure 8(B) through (D)), the displacement response at the corner point $A = (48, 20, 60)$ mm is evaluated for various nonlocal parameters l relative to the length of the geometry L. The compared elements are the proposed P1FB$_{\boldsymbol{H}}$-RT0$_{\boldsymbol{\Phi}}$-P0$_{\boldsymbol{\mu}}$ and P1FB$_{\boldsymbol{H}}$-RT0$_{\boldsymbol{\Lambda}}$-P0$_{\boldsymbol{\mu}}$ discretizations as well as the P2$_{\boldsymbol{u}}$-P2$_{\boldsymbol{H}}$-P1$_{\boldsymbol{\Lambda}}$ element from Reference 18, which again is based on a non-decoupled approach for the Lagrange mutliplier and $\psi^{\mathrm{loc}} := \psi^{\mathrm{loc}}(\nabla\boldsymbol{u})$ remaining a functional of $\boldsymbol{u}$ (cf. explanation in Section 4.1). From Figure 9(A) it can be seen, that for $l/L = 0$ the solution of the proposed formulations coincides with the converged solution $u_z(A) = 21.41$ mm of the local P$_{\boldsymbol{u}}$ displacement formulation. Note, that in this case for the element P1FB$_{\boldsymbol{H}}$-RT0$_{\boldsymbol{\Lambda}}$-P0$_{\boldsymbol{\mu}}$ (cf. Table 3) a stabilization parameter $\alpha = 10\ L$ yields sufficient results, while for the element P1FB$_{\boldsymbol{H}}$-RT0$_{\boldsymbol{\Phi}}$-P0$_{\boldsymbol{\mu}}$ a higher value $\alpha = 500\ L$ for the stabilization parameter is necessary to obtain results that are coinciding with the local converged solution. Moreover, in this case ($l/L = 0$) the Newton–Raphson solution procedure fails to converge for the P2$_{\boldsymbol{u}}$-P2$_{\boldsymbol{H}}$-P1$_{\boldsymbol{\Lambda}}$ element. Nevertheless, for $l/L \geq 0.05$ mm it can be seen from Figure 9(A), that for the three gradient elasticity elements the displacement response depending on l/L is similar. The dependency of the displacement response on the ratio l/L can be related to the modeling of size effects (cf. Reference 4). Similar to the 2D results of Section 4.2, the contour plot of Figure 8(C) also shows a reduction of the element average Cauchy stress for $l = 0.0005\ L$ at the singularity point $B = (0, 0, 44)$ mm compared to the local element P2$_{\boldsymbol{u}}$ (cf. Figure 8(B)). The computing time, which corresponds to the simulation marked with a bullet in Figure 9(A) is comparable for both elements, see Figure 9(B). Again, as in the numerical evaluation of the proposed

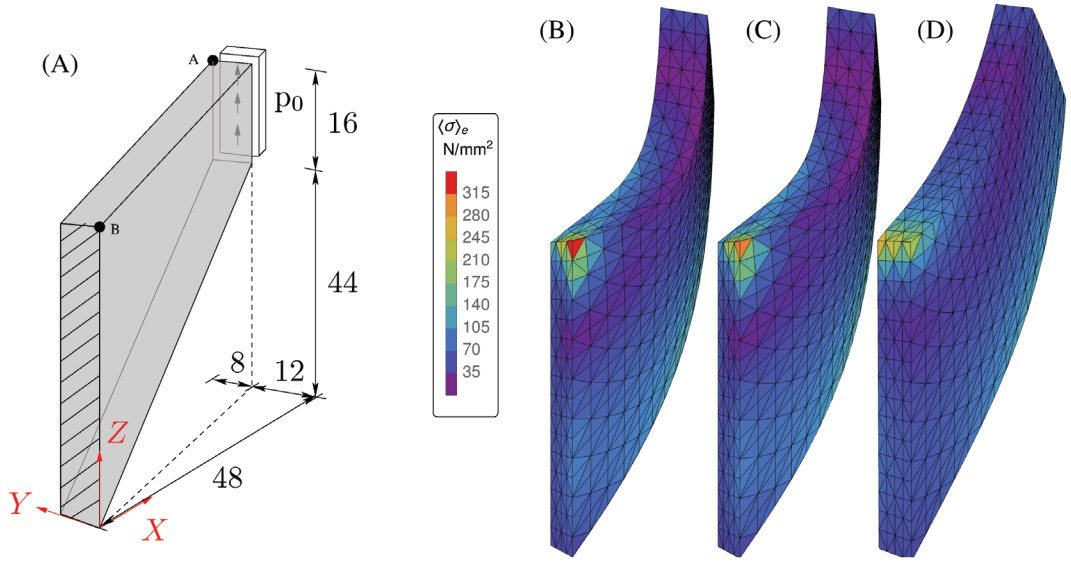

FIGURE 8 Three-dimensional Cook's problem: (A) geometry description. Non-smoothed $\langle \boldsymbol{\sigma} \rangle_e$ contour plots of the (B) local displacement element $\mathrm{P2}_{\boldsymbol{u}}$ and of the $\mathrm{P1FB}_{\boldsymbol{H}}$-$\mathrm{RT0}_{\boldsymbol{\Lambda}}$-$\mathrm{P0}_{\mu}$ element for (C) $l = 0.0005L$ and for (d) $l = 0.05L$

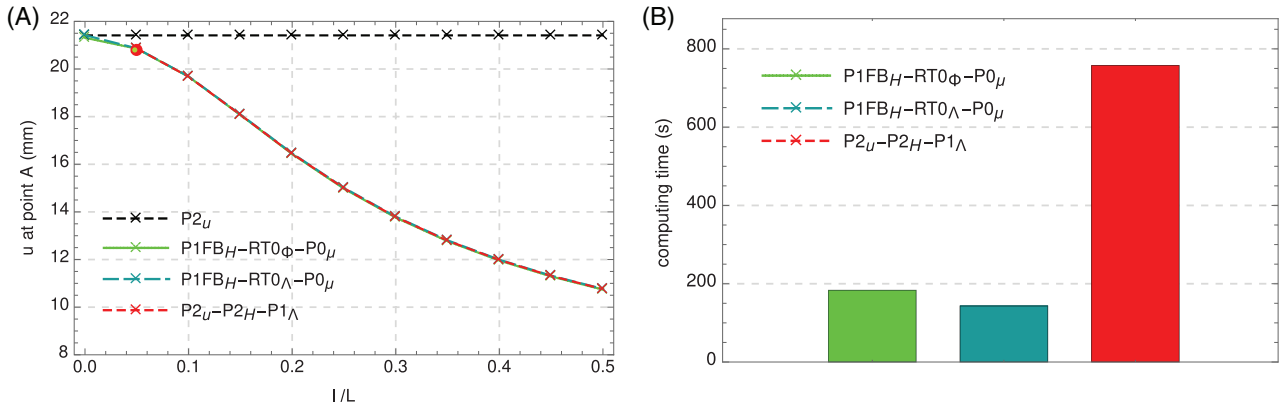

FIGURE 9 Size effect: (A) displacement response of the proposed elements and the $\mathrm{P2}_{\boldsymbol{u}}$-$\mathrm{P2}_{\boldsymbol{H}}$-$\mathrm{P1}_{\boldsymbol{\Lambda}}$ element from Reference 18 versus varying values of nonlocal parameter l relative to the domain size L; (B) comparison of computing time corresponding to the simulation marked with a bullet in (A). Depicted are results of a mesh refinement stage corresponding to 5120 elements (cf. contour plots Figure 8)

2D formulations (cf. Section 4.1.3) a reduced computing time compared to the nondecoupled $\mathrm{P2}_{\boldsymbol{u}}$-$\mathrm{P2}_{\boldsymbol{H}}$-$\mathrm{P1}_{\boldsymbol{\Lambda}}$ element can be observed.

5 | CONCLUSION

A new C^0-continuous mixed finite element formulation for finite strain gradient elasticity was introduced. The proposed approach was based on a split of the constraint term, which enforces compatibility between the mixed variables. As a result, a set of decoupled variational equations was obtained. In the linear setting, stability of the corresponding continuous formulation was proven. Robustness was shown even in the limit case of a vanishing nonlocal contribution and corresponding suitable finite element discretizations were introduced both in the 2D and the 3D case. Numerical tests of the nonlinear finite strain formulation showed appropriate convergence behavior and robustness of the proposed finite elements. The computing time was compared to the 2D three-field approach of Reference 18 (see also Reference 16) and a notable cost reduction was shown.

ACKNOWLEDGEMENTS

The authors greatly appreciate financial funding by the German Science Foundation (Deutsche Forschungsgemeinschaft, DFG), as part of the Priority Program 1748 "Reliable simulation techniques in solid mechanics. Development of non-standard discretisation methods, mechanical and mathematical analysis", project IDs BA2823/15-1, SCHE1885/1-1. Open access funding enabled and organized by Projekt DEAL.

ORCID

Daniel Balzani https://orcid.org/0000-0002-1422-4262

REFERENCES

1. Cosserat E, Cosserat F. Théorie des corps déformables. *Nature*. 1909;81:67.
2. Neff P, Jeong J, Münch I, Ramezani H. Chapter 6 Linear cosserat elasticity, conformal curvature and bounded stiffness. *Mechanics of Generalized Continua: One Hundred Years After the Cosserats*. New York, NY: Springer; 2010:55-63.
3. Mindlin R. Micro-structure in linear elasticity. *Arch Ration Mech Anal*. 1964;16:51-78.
4. Askes H, Aifantis EC. Gradient elasticity in statics and dynamics: an overview of formulation, length scale identification procedures, finite element implementations and new results. *Int J Solids Struct*. 2011;48:1962-1990.
5. Eringen AC. *Microcontinuum Field Theories I: Foundations and Solids*. New York, NY: Springer; 1999.
6. Abali BE, Müller WH, dell'Isola F. Theory and computation of higher gradient elasticity theories based on action principles. *Arch Appl Mech*. 2017;87:1495-1510.
7. Yang H, Abali BE, Timofeev D, Müller WH. Determination of metamaterial parameters by means of a homogenization approach based on asymptotic analysis. *Contin Mech Thermodyn*. 2019;32:1251-1270. https://doi.org/10.1007/s00161-019-00837-4.
8. Wang B, Yijia G, Shujun Z, Long-Qing C. Flexoelectricity in solids: progress, challenges, and perspectives. *Prog Mater Sci*. 2019;106:100570.
9. Papanicolopulos S, Zervos A, Vardoulakis I. A three-dimensional C^1 finite element for gradient elasticity. *Int J Numer Methods Eng*. 2008;77:1396-1415.
10. Rudraraju S, Van der Ven A, Garikipati K. Three-dimensional isogeometric solutions to general boundary value problems of Toupin's gradient elasticity theory at finite strains. *Comp Methods Appl Mech Eng*. 2014;278:705-728.
11. Liu C, Wang J, Xu G, Kamlah M, Zhang TY. An isogeometric approach to flexoelectric effect in ferroelectric materials. *Int J Solids Struct*. 2019;162(1):198-210.
12. Nguyen BH, Zhuang X, Rabczuk T. NURBS-based formulation for nonlinear electro-gradient elasticity in semiconductors. *Comp Methods Appl Mech Eng*. 2018;346:1074-1095.
13. Zervos A. Finite elements for elasticity with microstructure and gradient elasticity. *Int J Numer Methods Eng*. 2008;73:564-595.
14. Papanicolopulos S, Gulib F, Marinelli A. A novel efficient mixed formulation for strain-gradient models. *Int J Numer Methods Eng*. 2018;117(8):926-937.
15. Reiher JC, Giorgio I, Bertram A. Finite-element analysis of polyhedra under point and line forces in second-strain gradient elasticity. *J Eng Mech*. 2016;143(2):040616112.
16. Shu JY, King WE, Fleck NA. Finite elements for materials with strain gradient effects. *Int J Numer Meth Eng*. 1999;44:373-391.
17. Zybell L, Mühlich U, Kuna M, Zhang ZL. A three-dimensional finite element for gradient elasticity based on a mixed-type formulation. *Comput Mater Sci*. 2012;52:268-273.
18. Riesselmann J, Ketteler JW, Schedensack M, Balzani D. Three-field mixed finite element formulation for gradient elasticity at finite strains. *GAMM Mitteilungen*. Hoboken, NJ: Wiley; 2020:e202000002.
19. Gallistl D. Stable splitting of polyharmonic operators by generalized stokes systems. *Math Comput*. 2017;86(308):2555-2577.
20. Pauly D, Zulehner W. On closed and exact Grad-grad- and div-Div-complexes, corresponding compact embeddings for tensor rotations, and a related decomposition result for biharmonic problems in 3d; 2017. Preprint, arXiv:1609.05873v4.
21. Toupin R. Theories of elasticity with couple-stress. *Arch Ration Mech Anal*. 1964;17:85-112.
22. Washizu K. *Variational Methods in Elasticity and Plasticity*. 2nd ed. New York: Pergamon Press; 1975.
23. Ortiz M, Morris GR. C^0 finite element discretization of Kirchhoff's equations of thin plate bending. *Int J Numer Methods Eng*. 1988;26:1551-1566.
24. Boffi D, Brezzi F, Fortin M. *Mixed Finite Element Methods and Applications, volume 44 of Springer Series in Computational Mathematics*. Heidelberg, Germany: Springer; 2013.
25. Braess D. *Finite Elementes: Theory, Fast Solvers, and Applications in Solid Mechanics*. New York, NY: Springer; 2007.
26. Arnold D, Brezzi F. Mixed and nonconforming finite element methods: implementation, postprocessing and error estimates. *Math Anal Numer*. 1985;19(1):7-32.
27. Raviart PA, Thomas JM. A mixed finite element method for 2-nd order elliptic problems. *Mathematical Aspects of Finite Element Methods, Lecture Notes in Mathematics*; Berlin, Heidelberg: Springer; 1977;606:292-315.
28. Korelc J, Wriggers P. *Automation of Finite Element Methods*. New York, NY: Springer; 2016.
29. Ciarlet PG. *Mathematical Elasticity I: Three-Dimensional Elasticity*. Amsterdam: Elsevier Science Ltd; North Holland; 1988.
30. Wriggers P. *Nonlinear Finite Element Methods*. New York, NY: Springer; 2008.

31. Triantafyllidis N, Aifantis EC. A gradient approach to localization of deformation I. hyperelastic materials. *J Elast*. 1986;16:225-237.
32. Viebahn N, Steeger K, Schröder J. A simple and efficient Hellinger-Reissner type mixed finite element for nearly incompressible elasticity. *Comp Methods Appl Mech Eng*. 2018;340:278-295.
33. Amrouche C, Girault V. Problèmes généralisés de Stokes. *Port Math*. 1992;49(4):463-503.
34. Lou Z, McIntosh A. Hardy space of exact forms on R^{N}. *Trans Am Math Soc*. 2005;357(4):1469-1496.
35. Brezzi F. On the existence, uniqueness and approximation of saddle-point problems arising from Lagrangian multipliers. *Rev Française Automat Informat Recherche Opérationnelle Sér Rouge*. 1974;8(R-2):129-151.

How to cite this article: Riesselmann J, Ketteler JW, Schedensack M, Balzani D. Rot-free mixed finite elements for gradient elasticity at finite strains. *Int J Numer Methods Eng*. 2021;1–27. https://doi.org/10.1002/nme.6592

APPENDIX A. INTERPOLATION MATRICES

In this section we give some notes on the construction of the interpolation matrices used in Section 3.2. The element shape functions are constructed in the coordinates of the reference triangle and tetrahedron respectively. By means of the affine transformation from the reference coordinate space to the physical coordinate space, the well-known kinematics for the gradient operator are given by $\nabla(\bullet) = \boldsymbol{J}^{-T}\nabla_{\xi}(\bullet)$, where $\boldsymbol{J}$ is the Jacobian matrix and ∇_{ξ} denotes the gradient with respect to the coordinate system of the reference element. Moreover, the kinematic relation of the divergence operator is given by

$$\mathrm{Div}(\bullet) = \frac{1}{\det \boldsymbol{J}}\mathrm{Div}_{\xi}(\bullet). \tag{A1}$$

A.1 Lagrange interpolation matrices

The following relations illustrate the transition from the tensor notation to the matrix notation.

$$\begin{aligned}
\boldsymbol{u}^h &= \sum_I \boldsymbol{d}_u^I N_I \qquad &\Rightarrow \qquad \underline{\boldsymbol{u}}^h &= \underline{\boldsymbol{N}}_u \underline{\boldsymbol{d}}_u,\\
\boldsymbol{H}^h &= \sum_I \boldsymbol{d}_H^I N_I \qquad &\Rightarrow \qquad \underline{\boldsymbol{H}}^h &= \underline{\boldsymbol{N}}_H \underline{\boldsymbol{d}}_H,\\
\nabla\boldsymbol{u}^h &= \sum_I \boldsymbol{d}_u^I \otimes \nabla N_I \qquad &\Rightarrow \qquad \nabla\underline{\boldsymbol{u}}^h &= \underline{\boldsymbol{B}}_u \underline{\boldsymbol{d}}_u,\\
\nabla\boldsymbol{H}^h &= \sum_I \boldsymbol{d}_H^I \otimes \nabla N_I \qquad &\Rightarrow \qquad \nabla\underline{\boldsymbol{H}}^h &= \underline{\boldsymbol{B}}_H \underline{\boldsymbol{d}}_H.
\end{aligned}$$

Here, the left column represents a representation in tensor notation, where $\boldsymbol{d}_{(\bullet)}^I$ depicts the vector/tensor of degrees of freedom and N_I the Lagrangian shape function corresponding to the I-th element node. In the matrix notation, the solution variables (e.g., $\underline{\boldsymbol{H}}^h, \nabla\underline{\boldsymbol{H}}^h, \dots$) and associated element-wise collections of nodal degrees of freedom ($\underline{\boldsymbol{d}}_H, \underline{\boldsymbol{d}}_u \dots$) are considered to be column-matrices while the element-wise interpolation operators (eg. $\underline{\boldsymbol{N}}_H, \underline{\boldsymbol{B}}_H, \dots$) are matrix quantities. Moreover, in order to simplify the notation with respect to the assembly procedure (cf. (53),(57) and (61)) they are assumed to be in the dimension of the global system. The piecewise constant interpolation of the second Lagrange multiplier variable of Section 3.2 is performed analougously through

$$\boldsymbol{\mu}^h = \boldsymbol{d}_{\mu}^{\mathrm{in}} N_{\mathrm{in}}^{\mu} \qquad \Rightarrow \qquad \underline{\boldsymbol{\mu}}^h = \underline{\boldsymbol{N}}_{\mu} \underline{\boldsymbol{d}}_{\mu},$$

with $N_{\mathrm{in}}^{\mu} = 1$ and the vector $\boldsymbol{d}_{\mu}^{\mathrm{in}}$ corresponding to the degrees of freedom of the internal node of the element. For the construction of the rotation operator matrix the following relations are used:

$$\mathrm{Rot}\,\boldsymbol{H}^h = \begin{bmatrix} (\nabla\boldsymbol{H}^h)_{121} - (\nabla\boldsymbol{H}^h)_{112} \\ (\nabla\boldsymbol{H}^h)_{221} - (\nabla\boldsymbol{H}^h)_{212}. \end{bmatrix} \quad \text{for } d = 2 \qquad \Rightarrow \qquad \mathrm{Rot}\,\underline{\boldsymbol{H}}^h = \underline{\boldsymbol{R}}_H \underline{\boldsymbol{d}}_H \tag{A2}$$

and similarly for $d = 3$, the relation

$$\operatorname{Rot} \boldsymbol{H}^h = \begin{bmatrix} (\nabla \boldsymbol{H}^h)_{132} - (\nabla \boldsymbol{H}^h)_{123} & (\nabla \boldsymbol{H}^h)_{113} - (\nabla \boldsymbol{H}^h)_{131} & (\nabla \boldsymbol{H}^h)_{121} - (\nabla \boldsymbol{H}^h)_{112} \\ (\nabla \boldsymbol{H}^h)_{232} - (\nabla \boldsymbol{H}^h)_{223} & (\nabla \boldsymbol{H}^h)_{213} - (\nabla \boldsymbol{H}^h)_{231} & (\nabla \boldsymbol{H}^h)_{221} - (\nabla \boldsymbol{H}^h)_{212} \\ (\nabla \boldsymbol{H}^h)_{332} - (\nabla \boldsymbol{H}^h)_{323} & (\nabla \boldsymbol{H}^h)_{313} - (\nabla \boldsymbol{H}^h)_{331} & (\nabla \boldsymbol{H}^h)_{321} - (\nabla \boldsymbol{H}^h)_{312} \end{bmatrix}, \tag{A3}$$

is used.

A.2 Raviart–Thomas interpolation matrices

Similarly to the preceding explanations, the Raviart–Thomas interpolation matrices can be constructed from the following relations.

$$\boldsymbol{\Phi}^h = \sum_I \boldsymbol{d}_\Phi^I \otimes \Psi_I \qquad \Rightarrow \qquad \underline{\boldsymbol{\Phi}}^h = \underline{\boldsymbol{S}}_\Phi \underline{\boldsymbol{d}}_\Phi$$

$$\operatorname{Div} \boldsymbol{\Phi}^h = \sum_I \boldsymbol{d}_\Phi^I \operatorname{Div} \Psi_I \qquad \Rightarrow \qquad \operatorname{Div} \underline{\boldsymbol{\Phi}}^h = \underline{\boldsymbol{D}}_\Phi \underline{\boldsymbol{d}}_\Phi$$

Here, the nodal degrees of freedom $\boldsymbol{d}_\Phi^I$ correspond to the first moment of the element-surface normal direction of the solution variable.[27] Moreover, Ψ_I depicts the lowest order Raviart–Thomas shape function in the physical coordinate space corresponding to the Ith mid-face element node. Opposed to the Lagrange interpolation operators, the Raviart–Thomas shape functions are additionally mapped via Piola transformation from the reference coordinate space to the physical coordinate space (for a description on the construction of Ψ_I see Reference 32).

APPENDIX B. PROOFS

In this section proofs of the propositions and lemmas of the mathematical analysis of Section 3 are given. The proofs are listed in the order as the corresponding propositions etc. appear in the text.

Proof of Proposition 1. To prove proposition 1 we use the following proposition. ∎

Proposition 7. *Let $d \in \{2, 3\}$. If $d = 3$, let $\mathcal{B}$ be contractible. For all c_1 and α with $\max\{c_1, \alpha\} < C < \infty$ the bilinear form b satisfies the inf-sup condition*

$$\sup_{\delta \boldsymbol{H} \in \mathcal{V} \setminus \{0\}} \frac{b(\delta \boldsymbol{H}, \delta \boldsymbol{\Phi})_{L^2(\mathcal{B})}}{|\!|\!| \delta \boldsymbol{H} |\!|\!|} \gtrsim \|\delta \boldsymbol{\Phi}\|_{L^2(\mathcal{B})}, \tag{B1}$$

for all $\delta \boldsymbol{\Phi} \in \mathcal{Q}$, where the constant hidden in $\gtrsim$ only depends on the upper bound C of c_1 and α, but not on c_1 and α itself.

Proof. Let first $d = 2$. Given some $\delta \boldsymbol{H} \in H_0^1(\mathcal{B}; \mathbb{R}^{2\times 2})$, define $\widetilde{\delta \boldsymbol{H}} \in H_0^1(\mathcal{B}; \mathbb{R}^{d\times d})$ by

$$\widetilde{\delta \boldsymbol{H}}_{i,2} := \delta \boldsymbol{H}_{i,1} \quad \text{and} \quad \widetilde{\delta \boldsymbol{H}}_{i,1} := -\delta \boldsymbol{H}_{i,2} \quad \text{for } i = 1, 2.$$

Then $\operatorname{rot} \delta \boldsymbol{H} = \operatorname{div} \widetilde{\delta \boldsymbol{H}}$ and $\|\delta \boldsymbol{H}\|_{H^1(\mathcal{B})} = \|\widetilde{\delta \boldsymbol{H}}\|_{H^1(\mathcal{B})}$. Since $|\!|\!| \bullet |\!|\!| \lesssim \| \bullet \|_{H^1(\mathcal{B})}$ with a constant hidden in $\lesssim$ only depending on the upper bound of c_1 and α, this implies

$$\begin{aligned} \sup_{\delta \boldsymbol{H} \in \mathcal{V} \setminus \{0\}} \frac{(\operatorname{rot} \delta \boldsymbol{H}, \delta \boldsymbol{\Phi})_{L^2(\mathcal{B})}}{|\!|\!| \delta \boldsymbol{H} |\!|\!|} &\gtrsim \sup_{\delta \boldsymbol{H} \in \mathcal{V} \setminus \{0\}} \frac{(\operatorname{rot} \delta \boldsymbol{H}, \delta \boldsymbol{\Phi})_{L^2(\mathcal{B})}}{\|\delta \boldsymbol{H}\|_{H^1(\mathcal{B})}} \\ &= \sup_{\widetilde{\delta \boldsymbol{H}} \in \mathcal{V} \setminus \{0\}} \frac{(\operatorname{div} \widetilde{\delta \boldsymbol{H}}, \delta \boldsymbol{\Phi})_{L^2(\mathcal{B})}}{\|\widetilde{\delta \boldsymbol{H}}\|_{H^1(\mathcal{B})}}. \end{aligned}$$

The Ladyzhenskaya lemma (compare Reference 33) implies

$$\sup_{\widetilde{\delta \boldsymbol{H}} \in \mathcal{V} \setminus \{0\}} \frac{(\operatorname{div} \widetilde{\delta \boldsymbol{H}}, \delta \boldsymbol{\Phi})_{L^2(\mathcal{B})}}{\|\widetilde{\delta \boldsymbol{H}}\|_{H^1(\mathcal{B})}} \gtrsim \|\delta \boldsymbol{\Phi}\|_{L^2(\mathcal{B})}.$$

This proves the assertion for $d = 2$.

Let now $d = 3$. Due to (Reference 34, proposition A.1) for each $\delta\boldsymbol{\Phi} \in \mathcal{Q}$ there is a $\varphi \in \mathcal{V}$ with $\delta\boldsymbol{\Phi} = \operatorname{rot}\varphi$ and $||\varphi||_{H^1(\mathcal{B})} \leq c||\delta\boldsymbol{\Phi}||_{L^2(\mathcal{B})}$ with a constant $c < \infty$. Since $|||\bullet||| \lesssim ||\bullet||_{H^1(\mathcal{B})}$ as above, we obtain for the choice $\delta\boldsymbol{H} = \varphi$

$$\sup_{\delta\boldsymbol{H}\in\mathcal{V}\setminus\{0\}} \frac{(\operatorname{rot}\delta\boldsymbol{H}, \delta\boldsymbol{\Phi})_{L^2(\mathcal{B})}}{|||\delta\boldsymbol{H}|||} \gtrsim \sup_{\delta\boldsymbol{H}\in\mathcal{V}\setminus\{0\}} \frac{(\operatorname{rot}\delta\boldsymbol{H}, \delta\boldsymbol{\Phi})_{L^2(\mathcal{B})}}{||\delta\boldsymbol{H}||_{H^1(\mathcal{B})}} \geq \frac{(\operatorname{rot}\varphi, \delta\boldsymbol{\Phi})_{L^2(\mathcal{B})}}{||\varphi||_{H^1(\mathcal{B})}}$$
$$\geq \frac{1}{c}\frac{\|\delta\boldsymbol{\Phi}\|^2_{L^2(\mathcal{B})}}{||\delta\boldsymbol{\Phi}||_{L^2(\mathcal{B})}} = \frac{1}{c}||\delta\boldsymbol{\Phi}||_{L^2(\mathcal{B})}.$$

This completes the proof. ∎

Proposition 7 is the main ingredient of the following proof of proposition 1.

Proof of Proposition 1. The definition of the norm $|||\bullet|||$ implies that $\tilde{a}$ is continuous and coercive on $\mathcal{V}$ with respect to $|||\bullet|||$. Furthermore, b is continuous with respect to the norm $|||\bullet|||$ on $\mathcal{V}$ and the $L^2(\mathcal{B})$ norm on $\mathcal{Q}$ with continuity constant $\min\{\alpha^{-1}, c_1^{-1}\}$. The inf-sup condition of b is proved in Proposition 7. Therefore, Brezzi's splitting theorem[35] implies the unique existence of solutions. ∎

Proof of Proposition 2. Let $(\boldsymbol{u}, \boldsymbol{H}, \boldsymbol{\Phi}, \boldsymbol{g}) \in \mathcal{G}\times\mathcal{V}\times\mathcal{Q}\times\mathcal{G}$ solve (17), (37) and (20). Then $b(\boldsymbol{H}, \delta\boldsymbol{\Phi}) = 0$ for all $\delta\boldsymbol{\Phi} \in \mathcal{Q}$ implies that $\operatorname{Rot}\boldsymbol{H} = 0$. Therefore, there exists some $\boldsymbol{w} \in \mathcal{V}$ such that $\boldsymbol{H} = \nabla\boldsymbol{w}$. Then (20) implies that $\boldsymbol{w} = \boldsymbol{u}$. For $\delta\boldsymbol{u} \in \mathcal{U}$, it holds that $\nabla\delta\boldsymbol{u} \in \mathcal{V}$ is an admissible test function in (37). This and $\operatorname{Rot}\nabla\delta\boldsymbol{u} = 0$ leads to

$$a(\nabla\boldsymbol{u}, \nabla\delta\boldsymbol{u}) = \tilde{a}(\boldsymbol{H}, \nabla\delta\boldsymbol{u}) = \tilde{a}(\boldsymbol{H}, \nabla\delta\boldsymbol{u}) + b(\nabla\delta\boldsymbol{u}, \boldsymbol{\Phi}) = (\nabla\boldsymbol{g}, \nabla\delta\boldsymbol{u})_{L^2(\mathcal{B})}.$$

Together with (17), this proves

$$a(\nabla\boldsymbol{u}, \nabla\delta\boldsymbol{u}) = \Pi^{\mathrm{ext}}[\delta\boldsymbol{u}].$$

Therefore, $\boldsymbol{u}$ solves (33). The other direction follows from this equivalence and the existence of unique solutions to (33) and (17), (37), and (20). ∎

Proof of Proposition 3. To prove Proposition 3 we need an abstract lemma, which generalizes Brezzi's splitting lemma[35] from a system with one constraint to a mixed system with two constraints. The lemma is also used in the stability analysis of Proposition 6.

Let $\mathcal{V}$, $\mathcal{Q}$, and $\mathcal{M}$ be Hilbert spaces with norms $\|\bullet\|_{\mathcal{V}}$, $\|\bullet\|_{\mathcal{Q}}$, and $\|\bullet\|_{\mathcal{M}}$ and let a, b, and c be bilinear forms on $\mathcal{V}\times\mathcal{V}$, $\mathcal{V}\times\mathcal{Q}$, $\mathcal{Q}\times\mathcal{M}$, respectively. We consider the abstract problem: Find $(\boldsymbol{H}, \boldsymbol{\Phi}, \boldsymbol{\mu}) \in \mathcal{V}\times\mathcal{Q}\times\mathcal{M}$ such that

$$\begin{aligned} a(\boldsymbol{H}, \delta\boldsymbol{H}) + b(\delta\boldsymbol{H}, \boldsymbol{\Phi}) &= (\nabla\boldsymbol{g}, \delta\boldsymbol{H})_{L^2(\mathcal{B})}, \\ b(\boldsymbol{H}, \delta\boldsymbol{\Phi}) + c(\delta\boldsymbol{\Phi}, \boldsymbol{\mu}) &= 0, \\ c(\boldsymbol{\Phi}, \delta\boldsymbol{\mu}) &= 0, \end{aligned} \tag{B2}$$

for all $(\delta\boldsymbol{H}, \delta\boldsymbol{\Phi}, \delta\boldsymbol{\mu}) \in \mathcal{V}\times\mathcal{Q}\times\mathcal{M}$.

The following lemma proves the stability of this system. ∎

Lemma 1 (Brezzi's splitting Lemma with two conditions). *Define the kernels of b and c by $Z(\mathrm{B}) := \{w \in \mathcal{V} : b(w, \delta\boldsymbol{\Phi}) = 0 \text{ for all } \delta\boldsymbol{\Phi} \in Z(C)\}$ and $Z(\mathrm{C}) := \{w \in \mathcal{Q} : c(w, \delta\boldsymbol{\mu}) = 0 \text{ for all } \delta\boldsymbol{\mu} \in \mathcal{M}\}$. Let a, b and c are continuous and a be symmetric and coercive on $Z(B)$, i.e., there exists a constant $C < \infty$ such that $a(\delta\boldsymbol{H}, \delta\boldsymbol{H}) \geq C\|\delta\boldsymbol{H}\|^2_{\mathcal{V}}$ for all $\delta\boldsymbol{H} \in Z(B)$. If furthermore*

$$\|\delta\boldsymbol{\mu}\|_{\mathcal{M}} \lesssim \sup_{\delta\boldsymbol{\Phi}\in\mathcal{Q}\setminus\{0\}} \frac{c(\delta\boldsymbol{\Phi}, \delta\boldsymbol{\mu})}{\|\delta\boldsymbol{\Phi}\|_{\mathcal{Q}}} \qquad \text{for all } \delta\boldsymbol{\mu} \in \mathcal{M},$$
$$\|\delta\boldsymbol{\Phi}\|_{\mathcal{Q}} \lesssim \sup_{\delta\boldsymbol{H}\in\mathcal{V}\setminus\{0\}} \frac{b(\delta\boldsymbol{H}, \delta\boldsymbol{\Phi})}{\|\delta\boldsymbol{H}\|_{\mathcal{V}}} \qquad \text{for all } \delta\boldsymbol{\Phi} \in Z(\mathrm{C}),$$

then problem (B2) has a unique solution $(\boldsymbol{H}, \boldsymbol{\Phi}, \boldsymbol{\mu}) \in \mathcal{V} \times \mathcal{Q} \times \mathcal{M}$ *and it satisfies*

$$\|\boldsymbol{H}\|_{\mathcal{V}} + \|\boldsymbol{\Phi}\|_{\mathcal{Q}} + \|\boldsymbol{\mu}\|_{\mathcal{M}} \lesssim \|\nabla \boldsymbol{g}\|_{\mathcal{V}^*}.$$

Proof. Define for all $(\boldsymbol{H}, \boldsymbol{\Phi})$ and $(\delta\boldsymbol{H}, \delta\boldsymbol{\Phi}) \in \mathcal{V} \times \mathcal{Q}$

$$\tilde{a}((\boldsymbol{H}, \boldsymbol{\Phi}), (\delta\boldsymbol{H}, \delta\boldsymbol{\Phi})) := a(\boldsymbol{H}, \delta\boldsymbol{H}) + b(\delta\boldsymbol{H}, \boldsymbol{\Phi}) + b(\boldsymbol{H}, \delta\boldsymbol{\Phi}).$$

From Brezzi's splitting lemma[35] and the assumptions of Lemma 1 we know that $\tilde{a}$ satisfies

$$\sup_{(\delta\boldsymbol{H}, \delta\boldsymbol{\Phi}) \in (\mathcal{Q} \times Z(\mathrm{C})) \setminus \{0\}} \frac{\tilde{a}((\boldsymbol{H}, \boldsymbol{\Phi}), (\delta\boldsymbol{H}, \delta\boldsymbol{\Phi}))}{\|\delta\boldsymbol{H}\|_{\mathcal{V}} + \|\delta\boldsymbol{\Phi}\|_{\mathcal{Q}}} \gtrsim \|\boldsymbol{H}\|_{\mathcal{V}} + \|\boldsymbol{\Phi}\|_{\mathcal{Q}},$$

for all $(\boldsymbol{H}, \boldsymbol{\Phi}) \in \mathcal{V} \times Z(C)$. Since $\tilde{a}$ is symmetric, the inf-sup condition with exchanged components follows as well. Define the bilinear form

$$\tilde{c}((\delta\boldsymbol{H}, \delta\boldsymbol{\Phi}), \delta\boldsymbol{\mu}) := c(\delta\boldsymbol{\Phi}, \delta\boldsymbol{\mu}) \qquad \text{for all } \delta\boldsymbol{H} \in \mathcal{V},\ \delta\boldsymbol{\Phi} \in \mathcal{Q},\ \delta\boldsymbol{\mu} \in \mathcal{M}.$$

Then the nullspace of the associated operator $\tilde{\mathrm{C}}$ is given by

$$\begin{aligned} Z(\tilde{\mathrm{C}}) &:= \{(\delta\boldsymbol{H}, \delta\boldsymbol{\Phi}) \in \mathcal{V} \times \mathcal{Q} : \tilde{c}((\delta\boldsymbol{H}, \delta\boldsymbol{\Phi}), \delta\boldsymbol{\mu}) = 0 \text{ for all } \delta\boldsymbol{\mu} \in \mathcal{M}\} \\ &= \mathcal{V} \times Z(\mathrm{C}). \end{aligned}$$

Thus, $\tilde{a}$ satisfies the inf-sup condition on $Z(\tilde{\mathrm{C}})$ and $\tilde{c}$ satisfies an inf-sup condition. An application of Brezzi's splitting lemma on $\tilde{a}$ and $\tilde{c}$ yields the assertion. ∎

We proceed with the proof of Proposition 3.

Proof of Proposition 3. Define the norm

$$\|\delta\boldsymbol{\Phi}\|_{H(\mathrm{Div})} := \left(\|\delta\boldsymbol{\Phi}\|^2_{L^2(\mathcal{B})} + \|\mathrm{Div}\,\delta\boldsymbol{\Phi}\|^2_{L^2(\mathcal{B})}\right)^{1/2},$$

on $\tilde{Q}$. Note that for $\delta\boldsymbol{\Phi} \in H^{1(2)}_0 \subseteq H(\mathrm{Div})$ it holds that $\|\delta\boldsymbol{\Phi}\|_{H(\mathrm{Div})} \lesssim \|\delta\boldsymbol{\Phi}\|_{H^1(\mathcal{B})}$. Therefore

$$\begin{aligned} \sup_{\delta\boldsymbol{\Phi} \in \tilde{Q} \setminus \{0\}} \frac{(\mathrm{Div}\,\delta\boldsymbol{\Phi}, \delta\boldsymbol{\mu})_{L^2(\mathcal{B})}}{\|\delta\boldsymbol{\Phi}\|_{H(\mathrm{Div})}} &\geq \sup_{\delta\boldsymbol{\Phi} \in H^{1(2)}_0 \setminus \{0\}} \frac{(\mathrm{Div}\,\delta\boldsymbol{\Phi}, \delta\boldsymbol{\mu})_{L^2(\mathcal{B})}}{\|\delta\boldsymbol{\Phi}\|_{H(\mathrm{Div})}} \\ &\gtrsim \sup_{\delta\boldsymbol{\Phi} \in H^{1(2)}_0 \setminus \{0\}} \frac{(\mathrm{Div}\,\delta\boldsymbol{\Phi}, \delta\boldsymbol{\mu})_{L^2(\mathcal{B})}}{\|\delta\boldsymbol{\Phi}\|_{H^1(\mathcal{B})}}. \end{aligned}$$

The inf-sup condition for the Stokes equations, also known as Ladyzhenskaya lemma,[33] proves

$$\sup_{\delta\boldsymbol{\Phi} \in H^{1(2)}_0 \setminus \{0\}} \frac{(\mathrm{Div}\,\delta\boldsymbol{\Phi}, \delta\boldsymbol{\mu})_{L^2(\mathcal{B})}}{\|\delta\boldsymbol{\Phi}\|_{H^1(\mathcal{B})}} \gtrsim \|\delta\boldsymbol{\mu}\|_{L^2(\mathcal{B})}.$$

This proves the inf-sup condition for the bilinear form $(\mathrm{Div}\,\bullet, \bullet)_{L^2(\mathcal{B})}$ on $\tilde{Q} \times \mathcal{M}$. The inf-sup condition for b is proved in Proposition 7. These two inf-sup conditions together with the continuity of all three involved bilinear forms and the coercivity of $\tilde{a}$ as in the proof of proposition 1 together with Lemma 1 yields the unique existence of solutions of (41).

If $(\boldsymbol{H}, \boldsymbol{\Phi}, \boldsymbol{\mu}) \in \mathcal{V} \times \tilde{Q} \times \mathcal{M}$ is a solution to (41), then $\mathrm{Div}\,\boldsymbol{\Phi} = 0$ and therefore $(\boldsymbol{H}, \boldsymbol{\Phi}) \in \mathcal{V} \times \mathcal{Q}$ is a solution to (37). The other direction of the equivalence follows from this and the unique existence of solutions for both problems. ∎

Proof of Proposition 4. The definition of the norm on $\hat{Q}$ implies

$$\sup_{\delta \boldsymbol{H} \in \mathcal{V} \setminus \{0\}} \frac{\langle \delta \boldsymbol{\Lambda}_{\mathrm{c}}, \delta \boldsymbol{H} \rangle}{|\!|\!| \delta \boldsymbol{H} |\!|\!|} = \| \delta \boldsymbol{\Lambda}_{\mathrm{c}} \|_{\hat{Q}},$$

which is the inf-sup condition of the bilinear form $\langle \bullet \, , \bullet \rangle$ in (44). This, the coercivity and continuity of a and the continuity of b prove together with Brezzi's splitting lemma the unique existence of solutions.

Let now $(\boldsymbol{H}, \boldsymbol{\Phi}) \in \mathcal{V} \times \mathcal{Q}$ be a solution to (37). Then $\langle \boldsymbol{\Lambda}_{\mathrm{c}}, \bullet \rangle := b(\bullet, \boldsymbol{\Phi})$ defines a bounded linear map from $\mathcal{V}$ to $\mathbb{R}$. Moreover, given $\varphi \in C_c^\infty(\mathcal{B})$, it holds that

$$\langle \operatorname{Div} \boldsymbol{\Lambda}_{\mathrm{c}}, \varphi \rangle := \langle \boldsymbol{\Lambda}_{\mathrm{c}}, \nabla \varphi \rangle = b(\nabla \varphi, \boldsymbol{\Phi}) = (\operatorname{Rot} \nabla \varphi, \boldsymbol{\Phi})_{L^2(\mathcal{B})} = 0.$$

This proves $\operatorname{Div} \boldsymbol{\Lambda}_{\mathrm{c}} = 0$ in the distributional sense and therefore $\boldsymbol{\Lambda}_{\mathrm{c}} \in \hat{Q}$. The definition of $\boldsymbol{\Lambda}_{\mathrm{c}}$ proves the first equation of (44). The equivalence of (37) with (33) from Proposition 2 implies that $\boldsymbol{H} = \nabla \boldsymbol{u}$. The definition of the divergence therefore leads for all $\delta \boldsymbol{\Lambda}_{\mathrm{c}} \in \hat{Q}$ to

$$\langle \delta \boldsymbol{\Lambda}_{\mathrm{c}}, \boldsymbol{H} \rangle = \langle \delta \boldsymbol{\Lambda}_{\mathrm{c}}, \nabla \boldsymbol{u} \rangle = \langle \operatorname{Div} \delta \boldsymbol{\Lambda}_{\mathrm{c}}, \boldsymbol{u} \rangle = 0,$$

which is the second equation of (44). The other direction follows from this equivalence and the unique existence of solutions to both problems. ∎

Proof of Proposition 5. The proof of Proposition 7 explains how a coordinate change transfers the inf-sup condition of the Stokes equations to the inf-sup condition for the bilinear form b. These arguments also prove the discrete inf-sup condition

$$\sup_{\delta \boldsymbol{H}^h \in \mathcal{V}^h \setminus \{0\}} \frac{(\operatorname{rot} \delta \boldsymbol{H}^h, \delta \boldsymbol{\Phi}^h)_{L^2(\mathcal{B})}}{\| \delta \boldsymbol{H}^h \|_{\mathcal{V}^h}} \gtrsim \| \delta \boldsymbol{\Phi}^h \|_{L^2(\mathcal{B})}.$$

As in Proposition 1, the bilinear form b is continuous, if $\alpha > C > 0$, and $\tilde{a}$ is continuous. Furthermore, the stabilization term in $\tilde{a}$ guarantees that $\tilde{a}$ is also coercive with respect to $|\!|\!| \bullet |\!|\!|$. The unique existence of solutions then follows from Brezzi's splitting lemma. The error estimate is a direct consequence of the stability of the discrete and the continuous problem. ∎

Proof of Proposition 6. The inf-sup condition of $(\operatorname{Div} \bullet, \bullet)_{L^2(\mathcal{B})}$ on $\mathcal{Q}^h \times \mathcal{M}^h$ is well-known.[25] Moreover, since $\operatorname{Div} \mathcal{Q}^h = \mathcal{M}^h$, the kernel reads $\mathcal{Q}^h \cap \mathcal{Q}$. Obviously, $\| \delta \boldsymbol{\Phi}^h \|_{L^2(\mathcal{B})} = \| \delta \boldsymbol{\Phi}^h \|_{H(\operatorname{Div})}$ for functions in $\mathcal{Q}^h \cap \mathcal{Q}$. This, $|\!|\!| \bullet |\!|\!| \lesssim \| \nabla \bullet \|_{L^2(\mathcal{B})}$ and the inf-sup condition

$$\sup_{\delta \boldsymbol{H}^h \in \mathcal{V}^h \setminus \{0\}} \frac{(\operatorname{rot} \delta \boldsymbol{H}^h, \delta \boldsymbol{\Phi}^h)_{L^2(\mathcal{B})}}{\| \nabla \delta \boldsymbol{H}^h \|_{L^2(\mathcal{B})}} \gtrsim \| \delta \boldsymbol{\Phi}^h \|_{L^2(\mathcal{B})} \qquad \text{for all } \ \delta \boldsymbol{\Phi}^h \in \mathcal{Q}^h \cap \mathcal{Q},$$

from Reference 19 prove the inf-sup condition

$$\sup_{\delta \boldsymbol{H}^h \in \mathcal{V}^h \setminus \{0\}} \frac{(\operatorname{rot} \delta \boldsymbol{H}^h, \delta \boldsymbol{\Phi}^h)_{L^2(\mathcal{B})}}{|\!|\!| \nabla \delta \boldsymbol{H}^h |\!|\!|} \gtrsim \| \delta \boldsymbol{\Phi}^h \|_{H(\operatorname{Div})} \qquad \text{for all } \ \delta \boldsymbol{\Phi}^h \in \mathcal{Q}^h \cap \mathcal{Q}.$$

This and the continuity of $\tilde{a}$ and b and the coercivity of $\tilde{a}$ (see also the proofs of proposition 1 and Proposition 5) together with Lemma 1 proves the unique existence of solutions. The error estimate is a consequence of the stability of the discrete and the continuous system and the fact that the discrete kernel of $(\operatorname{Div} \bullet, \bullet)_{L^2(\mathcal{B})}$ equals $\mathcal{Q}^h \cap \mathcal{Q} \subseteq \mathcal{Q}$. ∎